ISSN 2543-9901

JOURNAL OF CASTING & MATERIALS ENGINEERING

QUARTERLY
Vol. 10 No. 2/2026

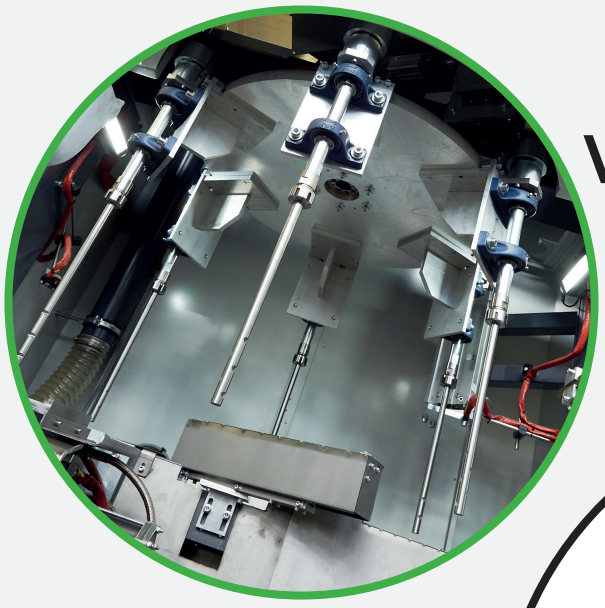

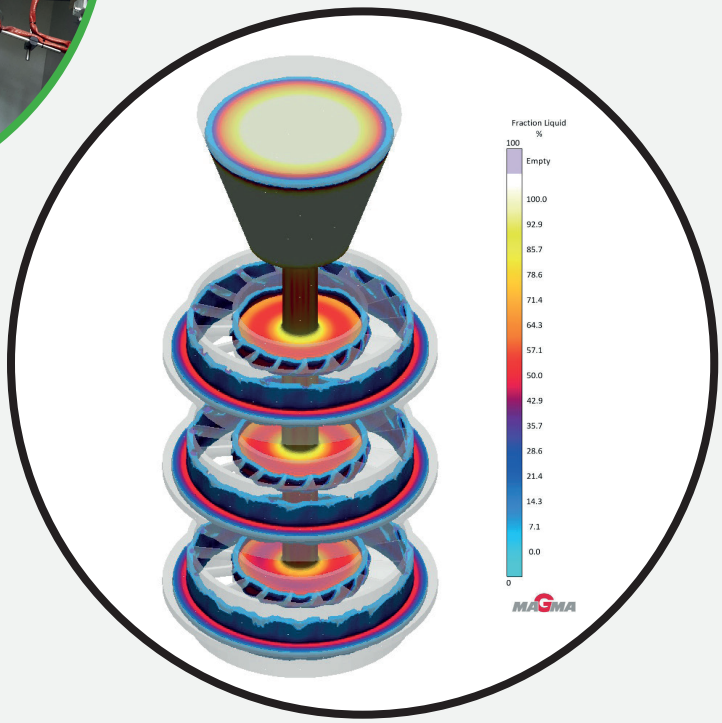

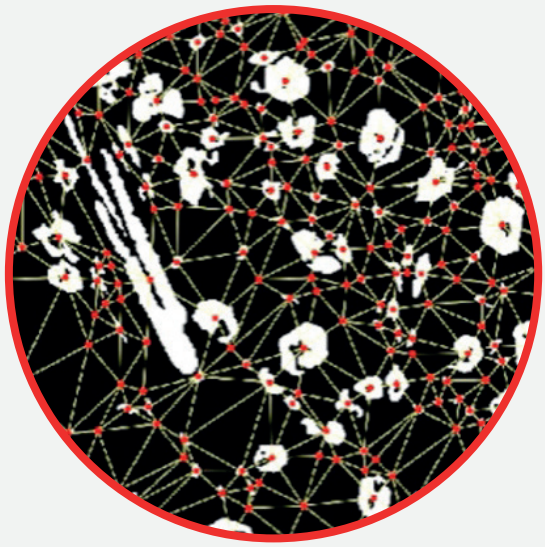

JCME

AGH UNIVERSITY OF KRAKOW
FACULTY OF FOUNDRY ENGINEERING

AGH UNIVERSITY PRESS
KRAKOW 2026

The articles published in the Journal of Casting & Materials Engineering have been given a favorable opinion by the reviewers designated by the Editorial Board.

www:
https://journals.agh.edu.pl/jcme/

AGH UNIVERSITY PRESS KRAKOW 2026

Wydawnictwa AGH (AGH University Press)
al. A. Mickiewicza 30, 30-059 Kraków
tel. 12 617 32 28, 12 638 40 38
e-mail: redakcja@wydawnictwoagh.pl
http://www.wydawnictwa.agh.edu.pl

Contents

Journal of Casting & Materials Engineering Vol. 10 No. 2 (2026) 30–33
https://doi.org/10.7494/jcme.2026.10.2.30

Comparison of Component Properties between HPDC and Rheocasting Applying the RheoMetal™ Process

Andreas Cziegler*

*Österreichisches Gießerei-Institut (Austrian Foundry Research Institute), Parkstraße 21, Leoben, Austria
e-mail: andreas.cziegler@ogi.at

Received: 16 April 2026/Accepted: 26 May 2026/Published online: 18 June 2026
This article is published with open access at AGH University of Krakow Journals

Abstract

Since the 1970s, there has been increasing interest in semi-solid processes, allowing improved mould filling with lower gas porosity and lower melt temperatures with improved tool life compared to the standard HPDC process. Challenges lie in the process know-how and the precise temperature control to ensure process stability and reproducibility. In contrast to other semi-solid processes, the RheoMetal™ process achieves the semi-solid state by stirring in an enthalpy exchange material (EEM). This work compares component properties (engine mount) produced by standard HPDC and rheocasting, applying the RheoMetal™ process using an AlSi7MnMg alloy. The results of component testing and radioscopic examination reveal promising outcomes regarding process stability, pore formation, and component properties compared to the standard HPDC process.

Keywords:

semi-solid processing, enthalpy exchange material, AlSi7MnMg, component testing, radioscopic examination

1. INTRODUCTION

Since the discovery of globular solidification in the 1970s by the research group led by M.C. Flemings [1], there has been strong and continuous interest in rheocasting processes. Advantages such as improved mould filling with reduced gas porosity, lower melt temperatures, and an increased tool life compared to the standard high-pressure die casting (HPDC) process have driven efforts to develop reliable and industrially scalable processes. These processes can generally be divided into thixocasting and rheocasting. The essential difference between thixocasting and rheocasting lies in the fact that thixocasting requires two separate process steps. Before the casting step, billets must be produced. These billets are then heated into the semi-solid region and cast into the mould. In contrast, rheocasting achieves the semi-solid state directly during the cooling phase of the melt, which is subsequently cast into the mould [2]. Compared to standard HPDC, rheocasting offers several significant advantages. The first positive aspect is the higher viscosity compared to fully liquid melts. This promotes the transition from turbulent to laminar flow, resulting in improved mould filling with fewer air and oxide inclusions. Secondly, less superheating is required. Consequently, the melt temperature can be kept lower, resulting in an increased tool lifetime, reduced sticking tendencies, and shorter solidification times. Another advantage is the formation of partially solidified melt, which can reduce volumetric shrinkage and enable near-net-shape production. Furthermore, castings with varying wall thickness can be produced more easily. Finally, the lower amount of gas porosity improves the suitability for heat treatment [3]. Among the challenges is the specific process know-how that is required in applying the rheocasting technology. Furthermore, precise temperature control is required, which is necessary because both the solid fraction and the viscosity are strongly dependent on the temperature [2], making rheocasting processes challenging with regard to process stability and reproducibility. Furthermore, slurry fabrication may result in an increase in production time [4]. To overcome the challenges of standard rheocasting processes, the RheoMetal™ [5] process was developed, which does not rely on complex temperature control but achieves the semi-solid state by stirring in an enthalpy exchange material (EEM). A liquid and solid alloy system is mixed together and with the help of stirring, the solid alloy a new alloy system (slurry) are produced with the targeted solid fraction. The initial temperature and composition of the melt and the EEM, and furthermore the amount of EEM, determine the final solid fraction, making precise temperature control during the process unnecessary. Furthermore, due to the rapid heat exchange between the cold EEM and the liquid melt, large amounts of semi-solid material can be produced in a short time [6, 7].

This work focuses on a comparison of component properties of parts produced by the RheoMetal™ process and the standard HPDC process.

2. MATERIALS AND METHODS

In this work, an AlSi7MnMg (Silafont®-33) alloy was used. Standard impeller degassing was applied with argon as the purge gas. The Bühler SC D/53 HPDC machine was equipped with a slurry maker to produce a maximum of 2 kg of slurry material (Comptech i Skillingaryd AB). An example engine mount (Fig. 1a, b) was cast both by standard HPDC and rheocasting. For the standard HPDC process, the machine is equipped with a vacuum dosing system using a dosing robot. In the case of rheocasting, a ladle is mounted to the dosing robot. Spraying of the die was performed with an automated spraying system, and the parts were removed manually.

The rheocasting process comprises the following steps:

1. casting of the required amount of melt around a steel rod to produce the EEM with a diameter of 40 mm and a height of 37 mm,
2. removal of the feeder and gating system,
3. extraction of the required amount of melt for the casting using a ceramic ladle,
4. stirring of the EEM into the melt,
5. homogenisation at a second stirring station, equipped with a non-dissolvable stirring rod,
6. filling of the semi-solid melt into the HPDC chamber,
7. cleaning of the steel rod.

The slurry maker is shown in Figure 1c. A stirring program was applied to produce slurry material with a solid fraction of approx. 24%.

The piston velocity of the second phase of the standard HPDC process was approx. 2.2 m/s. In contrast, rheocasting allows a lower piston velocity of the second phase due to the structural viscous behaviour of semi-solid melts. A piston velocity of the second phase of approx. 0.4 m/s for the rheocasting process was found to be appropriate for the engine mount used in this work.

A universal testing machine (Zwick 250 kN) for static applications was used for component testing of the individual casting parts. Each individual casting part was fixed on the clamping plate with 5 bolts. A press ram mounted on the universal testing machine was used to apply a compressive force on the opposite side of the engine mount (Fig. 1d). An initial load of 50 N and a testing speed of 20 mm/min were applied until failure of the individual casting part occurred. Above a piston stroke of 15 mm, the parts tend to be supported by the edge of the clamping plate. This effect is indicated by the increase in the compressive force, as shown in Figure 2a. Therefore, the compressive force at a piston stroke of 15 mm was used for the comparison of the individual casting parts.

Individual casting parts were also examined by radioscopic examination (v|tome|xc with a 240 kV microfocus X-ray).

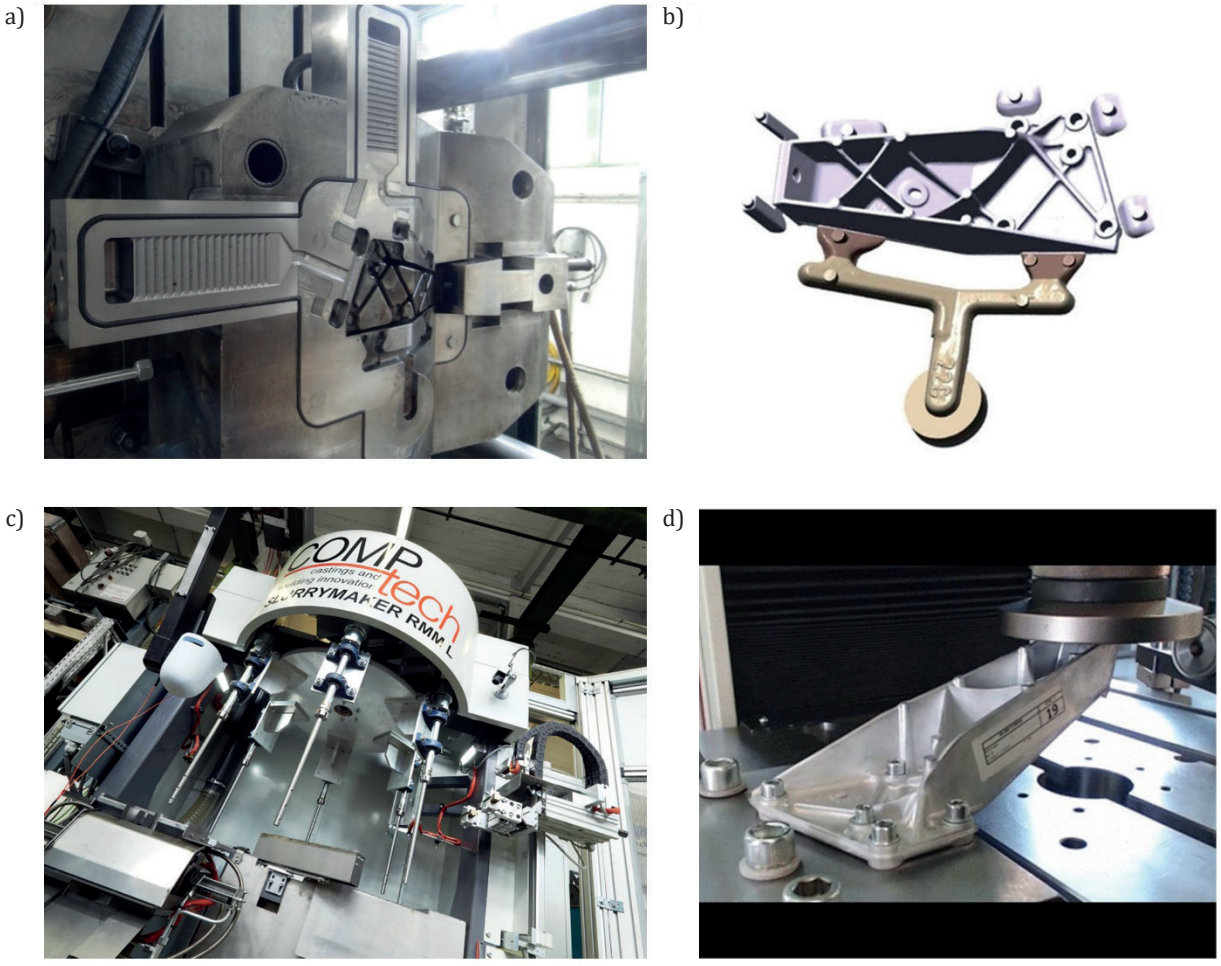

Fig. 1. Experimental facilities used in the present work: a) movable part of the mould; b) geometry of the engine mount; c) slurry maker from CompTech AB; d) engine mount component testing

3. RESULTS AND DISCUSSION

3.1. Component properties

The results of the component testing are shown in Figure 2. The compressive force of one individual casting part is shown versus punch stroke. The compressive force at a punch stroke of 15 mm was chosen for evaluation, as mentioned above; however, supporting the component on the specimen holder leads to an increase in compressive force beyond a piston stroke of 15 mm.

The results indicate that the parts produced by standard HPDC show a higher scattering compared to the parts produced by rheocasting applying the RheoMetal™ process. The mean value of the individual castings shows slightly higher component properties of the parts produced by rheocasting. The low scattering indicates that the RheoMetal™ process allows stable process conditions.

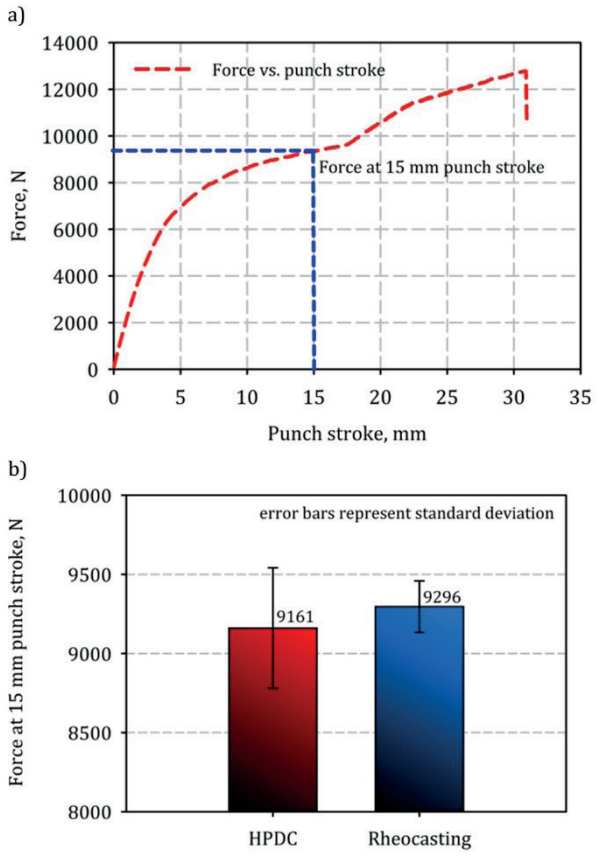

Fig. 2. Comparison of component testing between standard HPDC and rheocasting applying the RheoMetal™ process: a) schematic depiction of the compressive force vs. punch stroke; b) compressive force at 15 mm punch stroke of the individual castings produced by HPDC and rheocasting

3.2. Radioscopic examination

The results of individual castings investigated via radioscopic examination are shown in Figure 3. Oxide films and crack formation can be observed in both castings. (Fig. 3a, b for HPDC and Fig. 3c, d for rheocasting). In the HPDC part, oxide film formation can be attributed to turbulent melt flow in the region indicated by the blue arrow in Figure 3b.

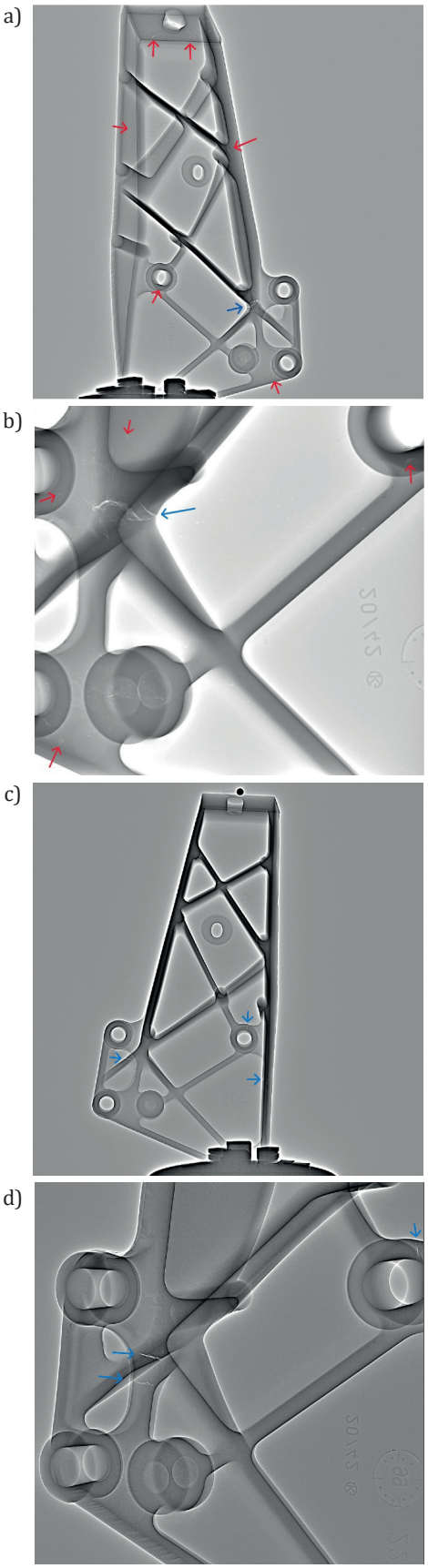

Fig. 3. Radioscopic images of individual casting parts: a) and b) standard HPDC; c) and d) rheocasting; less porosity in castings produced by rheocasting can be observed, indicated by red arrows; blue arrows indicate potential oxide films and crack formation, probably as a result of chilled melt fronts in the part produced by rheocasting

Crack formation in the part produced by rheocasting can be assumed to be a result of cold shut formation. Defects attributed to chilled melt fronts in rheocasting parts are also reported in the work by Richter et al. [8]. However, less gas porosity can be found in the part produced by rheocasting, which can be attributed to the more laminar melt flow of the rheocasting process. In the HPDC part, gas porosity, potentially associated with shrinkage porosity, is distributed across the entire component. This is also supported by the work of Granath et al. [9]. HPDC parts are prone to gas porosity, potentially connected with shrinkage porosity, whereas in parts produced by rheocasting, only shrinkage porosity potentially associated with oxide films can be observed.

4. CONCLUSION

Component testing of an engine mount was performed on samples produced by standard HPDC and rheocasting. The following conclusions can be drawn from the present work:

- Rheocasting enables a smoother mould filling compared to standard HPDC, with lower piston velocity – 0.4 m/s for rheocasting in contrast to 2.2 m/s for standard HPDC, resulting in a more laminar mould filling and less gas porosity, which also contributes to an increase in die lifetime.
- Component properties are comparable, showing a reduced scattering of the parts produced by rheocasting, indicating stable process conditions of the RheoMetal™ process.
- Lower porosity can be observed in castings performed by rheocasting.

The experimental investigations applying the RheoMetal™ process demonstrate promising outcomes and create scope for continued research and further optimisation efforts.

ACKNOWLEDGEMENTS

This work was supported by the FFG funding program 'Collective Research' (grant no. 915967).

DECLARATIONS

The author declares no competing interests of a financial or personal nature.

REFERENCES

[1] Flemings M.C., Riek R.G. & Young K.P. (1976). Rheocasting. *Materials Science and Engineering,* 25, 103–117. DOI: https://doi.org/10.1016/0025-5416(76)90057-4.

[2] Rosso M. (2012). Thixocasting and rheocasting technologies, improvements going on. *Journal of Achievements in Materials and Manufacturing Engineering,* 54(1), 110–119.

[3] Wessén M. & Cao H. (2007). The RSF technology – A possible breakthrough for semi-solid casting processes. *Metallurgical Science and Technology,* 25(2), 22–28.

[4] Payandeh M. (2016). *Rheocasting of Aluminium Alloys: Process and Components Characteristics* [doctoral dissertation]. Jönköping: Jönköping University.

[5] Cao H. & Wessén M. (2005). PCT/SE2005/001889. Jönköping: World Intellectual Property Organization.

[6] Jarfors A.E.W., Jafar M., Aqeel M., Liljeqvist P. & Jansson P. (2022). In-production rheometry of semi-solid metal slurries. *Metals,* 12(7), 1221, 1–13. DOI: https://doi.org/10.3390/met12071221.

[7] Cao H., Granath O. & Wessén M. (2008). The effect of Si content on the mechanical properties of rheocast Al components using the RHEOMETAL™ Process. *Solid State Phenomena*, 141–143, 779–784. DOI: https://doi.org/10.4028/www.scientific.net/SSP.141-143.779.

[8] Richter J., Wegener T., Schilling A., Fehlbier M. & Niendorf T. (2026). Rheocasting versus die casting: An insight into the low-cycle fatigue behavior of AlSi7Mg0.6. *Advanced Engineering Materials*, 28(4), e202502276, 1–12. DOI: https://doi.org/10.1002/adem.202502276.

[9] Granath O., Wessén M. & Cao H. (2010). Porosity reduction possibilities in commercial Aluminium A380 and Magnesium AM60 alloy components using the RheoMetal™ process. *Metallurgical Science and Technology*, 28(1), 2–11.

Journal of Casting & Materials Engineering Vol. 10 No. 2 (2026) 34–41
https://doi.org/10.7494/jcme.2026.10.2.34

Microstructure-Erosion Resistance Correlation in High Chromium Cast Iron: A Digital Image Processing Approach

Ottavia Vezzani[a], Annalisa Fortini[a]*, Michele Gragnanini[a], Alessio Suman[a], Nicola Zanini[a]

[a] University of Ferrara, Department of Engineering, Via Saragat 1, 44122 Ferrara, Italy
e-mail: annalisa.fortini@unife.it

Received: 20 April 2026/Accepted: 1 June 2026/Published online: 18 June 2026
This article is published with open access at AGH University of Krakow Journals.

Abstract

High chromium cast irons (HCCIs) are widely employed as wear-resistant hardfacing materials in industrial applications where solid particle erosion (SPE) represents a primary degradation mechanism, such as in energy production, mining, and cement manufacturing. The erosive wear resistance of these alloys is strongly dependent on the microstructural features of the primary M_7C_3 carbides, particularly their size, morphology, and spatial distribution within the metallic matrix. The quantitative relationship between carbide distribution homogeneity and erosion resistance has received limited attention in the literature. This study investigates the erosive wear resistance of a Fe-Cr-C cast iron hardfacing alloy and proposes three digital image processing methods to quantitatively characterise the carbide microstructure and correlate it with experimental erosion test results. Optical microscopy combined with image binarisation was used to segment primary M_7C_3 carbides. Three methods were adopted: carbide volume fraction (CVF), minimum inter-carbide distances, and a moving scanning area approach. Erosion tests were conducted according to ASTM G76 guidelines using two Arizona road dust powder grades with two mean diameters under equal kinetic energy conditions. Results show that the erosion rate decreases significantly with the increasing erodent particle size and that carbide distribution homogeneity plays a critical role in determining the erosion resistance. The moving scanning area method proved particularly effective at correlating microstructural coverage with experimental erosion rates.

Keywords:

chromium-rich carbides, hardfacing, image analysis, solid particle erosion, microstructural characterisation

1. INTRODUCTION

Extending the service life of mechanical components operating under severe surface degradation conditions is a major challenge across several industrial sectors, including energy production, mining, and bulk material handling. In applications where components are exposed to the impact of solid particles carried by a fluid stream, erosive wear is a primary failure mechanism, leading to progressive material removal and component replacement costs [1]. A widely adopted strategy to mitigate this problem is the application of hardfacing coatings deposited by welding onto critical surfaces, combining low process cost with the flexibility to treat localised areas and repair damaged zones without replacing entire components [1, 2].

Among hardfacing materials, high chromium cast irons (HCCIs) of the Fe-Cr-C family represent a well-established class of materials due to their hardness, wear and corrosion resistance, properties that are retained even at elevated temperatures [3, 4]. Their chemical composition typically ranges from 2 to 7 wt.% C and from 5 to 36 wt.% Cr and their microstructure consist of primary and eutectic carbides, predominantly of the M_7C_3 type (M = Cr, Fe), embedded in an austenitic, bainitic, or martensitic matrix [5]. The primary M_7C_3 carbides exhibit Vickers hardness values of 1300–1800 HV and serve as the primary barrier against wear, while the metallic matrix provides toughness and load-bearing support to the carbide network [6].

The morphology, size, and spatial distribution of carbides are recognised as critical factors governing the wear resistance of HCCIs [6, 7]. Primary M_7C_3 carbides can exhibit elongated or globular morphologies depending on the solidification conditions and alloy composition [8]. Elongated carbides tend to improve abrasive wear resistance, whereas globular carbides are generally associated with better impact resistance [9]. The carbide volume fraction (CVF), defined as the ratio of the area occupied by carbides to the total analysed area, is the parameter most used in the literature to characterise HCCIs and estimate their wear resistance [10]. Higher CVF values are generally associated with increased hardness and wear resistance, although an excessive CVF can reduce toughness if the matrix is not adequately balanced. CVF can be modified through compositional adjustments, for instance,

increasing the Cr content promotes the formation of M_7C_3 and $M_{23}C_6$ carbides, or through destabilisation heat treatments that influence secondary carbide precipitation and matrix hardness [11–13].

The erosive wear behaviour of metallic substrates under solid particle impact depends on multiple factors, including the particle velocity, shape, size, impact angle, and chemical composition of the erodent, as well as the substrate microstructure [14, 15]. Although the erosion resistance of HCCIs has been widely investigated experimentally and numerically [16], the quantitative relationship between microstructural parameters and erosion resistance remains insufficiently explored [7, 10, 17]. In particular, the spatial homogeneity of the carbide distribution, which determines the local probability of matrix exposure to erodent impact, has rarely been addressed through systematic image analysis approaches.

The present study aims to fill this gap by developing and comparing three digital image processing methods for the quantitative characterisation of primary M_7C_3 carbides in a Fe-Cr-C HCCI hardfacing alloy. The methods are correlated with experimental solid particle erosion test results obtained using two erodent powder grades selected based on microstructural inter-carbide distance analysis, in accordance with ASTM G76 guidelines. The results demonstrate that carbide distribution homogeneity, rather than CVF alone, is a key parameter controlling the erosion resistance under the tested conditions.

2. MATERIALS AND METHODS

2.1. Material and sample preparation

The material investigated in this study is a commercial Fe-Cr-C cast iron deposited by hardfacing welding onto a low-carbon steel substrate. The chemical composition of the alloy, determined by Glow Discharge Optical Emission Spectroscopy (GDOES, Spectruma Analytik GDS 650, Hof, Germany), is reported in Table 1. The alloy is hypereutectic, with a primary M_7C_3 carbide fraction solidifying before the eutectic reaction.

Samples with dimensions of 20 mm × 20 mm × 10 mm were prepared in accordance with the requirements of the erosion test bench described in Section 2.2. All samples analysed in this study were extracted from the same hardfacing deposit batch to ensure consistency of welding parameters and microstructural homogeneity across the experimental campaign. Prior to microstructural analysis, sample surfaces were chemically etched using Kalling's reagent (5 g $CuCl_2$, 100 ml HCl, 100 ml C_2H_5OH) for 5 seconds to reveal the structural constituents. Metallographic analysis was performed using a Leica DMi8 A optical metallographic microscope (Leica, Wetzlar, Germany).

2.2. Erosion tests

Solid particle erosion tests were conducted using a dedicated test bench designed in accordance with ASTM G76 guidelines [18]. The apparatus provides control of operational parameters, including the air flow rate, erodent powder feed rate, impact angle, and test duration. A detailed description of the test bench design and its validation is reported in previous works by the authors [19–21].

An impact angle of 15° was selected to simulate the most severe and operationally representative damage conditions for the hardfacing coating under investigation [21]. The erodent material used in all tests was Arizona road dust (ARD), a standardised commercial powder compliant with ISO 12103-1:2016, composed of SiO_2 (75%), Al_2O_3 (20%) and minor oxides (Mg, Fe, and others) [22]. This powder is widely employed in filtration system testing and machine degradation studies. Two powder grades were selected for the erosion tests: ARD Ultrafine (ARD UF) and ARD Medium (ARD M), with mean particle diameters of 4.8 μm and 25.5 μm, respectively. Scanning electron microscopy (SEM) images are shown in Figure 1.

The two powder grades were selected based on the results of the inter-carbide distance analysis described in Section 2.3, to investigate two distinct interaction regimes between erodent particles and substrate microstructure: (i) mean particle diameter smaller than the inter-carbide distance, and (ii) mean particle diameter larger than the inter-carbide distance.

Operational parameters, i.e. air flow rate, powder feed rate and test duration, were determined through computational fluid dynamics (CFD) simulations, maintaining equal kinetic energy conditions for the erodent particles across both test configurations [21]. The powder feed rate was set to 10 g/min. The erosion resistance was quantified through sample mass loss, measured using a Kern ABT 100-5NM precision analytical balance (Kern, Balingen, Germany) with a resolution of 0.01 mg. The erosion rate (ER) was calculated as the ratio between the mass lost by the eroded sample (μg) and the mass of the injected erodent (g), as expressed in Equation (1):

$$ER = \Delta m\_sample / m\_erodent \quad (1)$$

where: Δm_sample is the mass loss of the sample (μg), and m_erodent is the total mass of the erodent injected (g). Ten samples were tested for each condition to ensure the statistical reliability of the results.

Table 1
Chemical composition of the investigated Fe-Cr-C cast iron (wt.%, Fe balance)

C	Mn	Si	Cr	Mo	Nb	W	V	Fe
4.15	0.56	1.08	21.04	2.78	4.09	0.86	0.69	Bal.

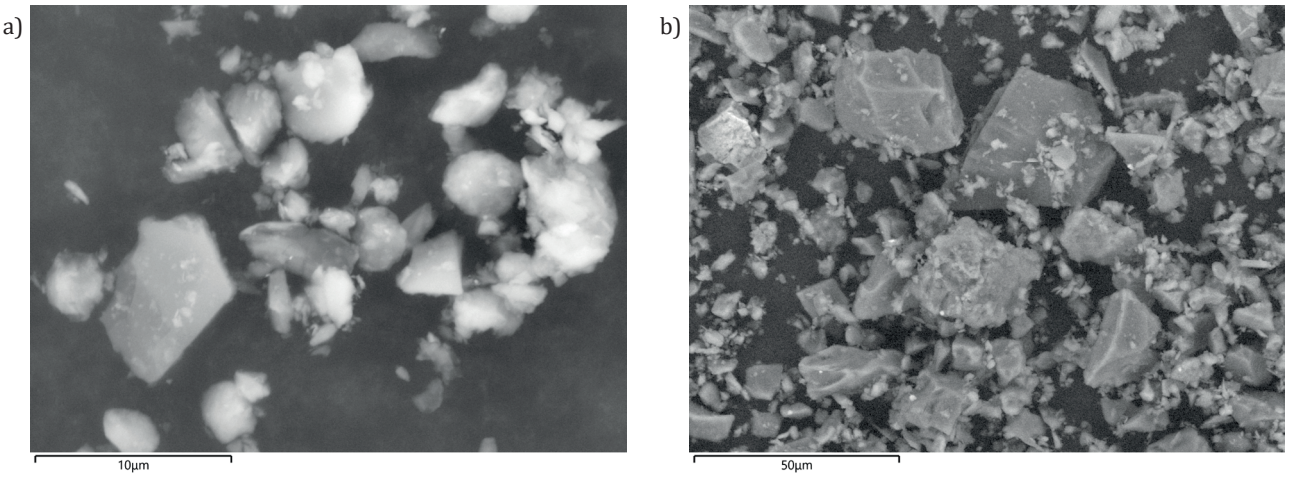

Fig. 1. SEM micrographs of the erodent powders used in the erosion tests: a) ARD UF (d_mean = 4.8 µm); b) ARD M (d_mean = 25.5 µm)

2.3. Microstructural analysis and image processing

Microstructural characterisation was performed on n = 10 samples, with n = 6 regions of interest (ROIs) identified on each sample, for a total analysed area of 9 mm^2 per sample. Micrographs were acquired at 200× magnification. The microstructure of the investigated alloy consists of polygonal primary M_7C_3 carbides surrounded by a predominantly austenitic matrix with traces of martensite and eutectic carbides. The alloy can therefore be regarded as a two-phase material with a composite-like structure in which the matrix provides toughness and the hard carbides act as reinforcement against wear.

Image processing was performed starting from optical micrographs, which were converted to binary black-and-white images by applying a grey-level threshold using the open-source software ImageJ (Version 1.53e, National Institutes of Health, USA) [23], as shown in Figure 2.

The chromatic contrast between carbides (bright) and matrix (dark) was exploited to segment the carbide phase. The binary images obtained served as the common input for the three analysis methods described as follows.

Method 1: carbide volume fraction (CVF). The carbide volume fraction is defined as the ratio of the total carbide area to the total analysed area, as expressed in Equation (2):

$$CVF = \Sigma\ A\_carbides\ /\ A\_total \quad (2)$$

where: A_carbides is the sum of the areas of all segmented carbide particles, and A_total is the total area of the analysed region. CVF was computed for each ROI across all samples using ImageJ, providing a mean value and associated variability for each region. This parameter represents the most widely used descriptor of HCCI microstructure in the wear literature [10] and serves as the baseline reference method in this study.

Method 2: Minimum inter-carbide distances via Delaunay triangulation. This method was developed to characterise the spatial distribution of primary carbides by computing the minimum edge-to-edge distances between adjacent carbides. Starting from the binary images (Fig. 3a), the centroid coordinates of each carbide particle were extracted after an image cleaning step to remove artifacts and eutectic carbides below a minimum size threshold, to reduce the computational load and focus the analysis on primary carbides (Fig. 3b). Carbide adjacency was determined through Delaunay triangulation applied to the centroid coordinates, and the validity of each triangulation link was verified geometrically to exclude connections crossing other carbide bodies (Fig. 3c).

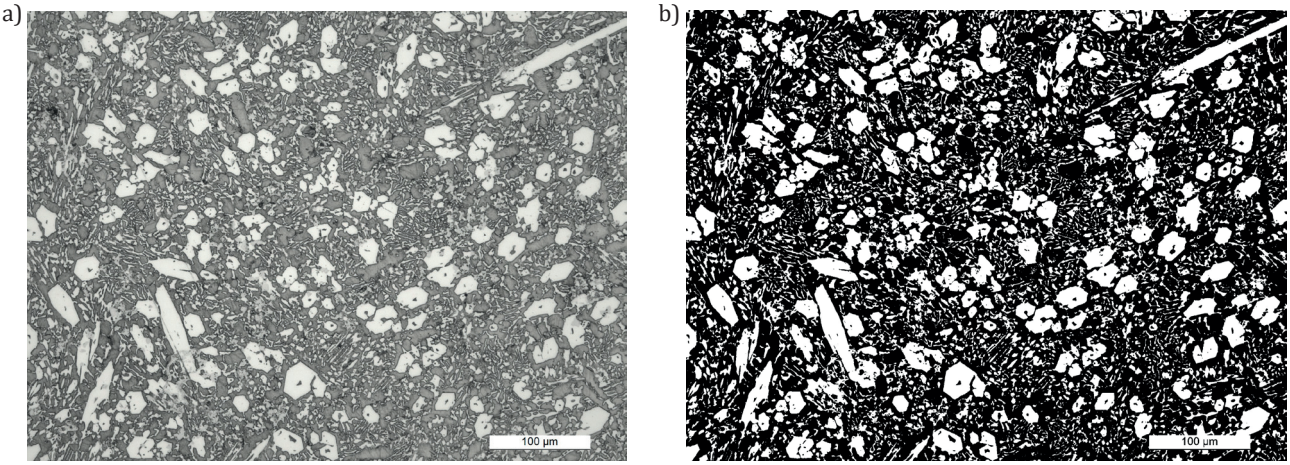

Fig. 2. Example of an optical micrograph of the material under examination: a) original image; b) post-processed binary version

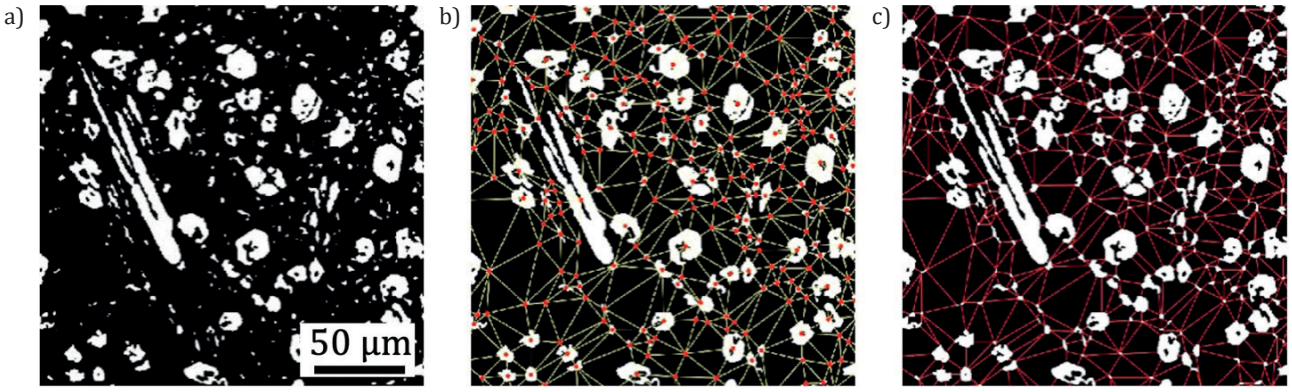

Fig. 3. Image processing steps for Method 2: a) binary image after cleaning; b) carbide centroid coordinates and Delaunay triangulation network with validity check of connections; c) final map of minimum edge-to-edge distances between adjacent carbides

For each valid pair of adjacent carbides, the minimum edge-to-edge distance was then computed as the shortest distance between the respective perimeters, using a dedicated Python script. The resulting distance distributions were represented as boxplot diagrams for each ROI, enabling direct comparison of inter-carbide spacing variability across different microstructural zones. This method provides information exclusively on the spatial homogeneity of the carbide distribution, independently of the carbide area fraction.

Method 3: Moving scanning area. This method was designed to simulate the impact of erodent particles on the substrate microstructure and to quantitatively assess the local carbide coverage experienced by an impacting particle. Starting from the binary images, a square sampling area with a side length equal to the mean equivalent diameter of the erodent powder was defined. The conversion from pixels to micrometres was performed based on the micrograph scale bar using ImageJ. The sampling area was systematically translated across the entire image by centring it on each sampling pixel, and for each position, the coverage ratio (*Rc*) was computed as the ratio of white pixels (carbides) to total pixels within the sampling area, as expressed in Equation (3):

$$Rc = \text{N\_white} / \text{N\_total} \quad (3)$$

where: N_white is the number of carbide pixels, and N_total is the total number of pixels in the sampling area. To manage the computational cost, a scanning step greater than 1 pixel can be adopted, meaning that the sampling pixel is shifted by a fixed number of pixels in both the horizontal and vertical directions between consecutive evaluations. Border effects were avoided by excluding sampling positions within half the equivalent diameter of the image edges. The procedure was implemented in a Python script, and the output is a frequency histogram of *Rc* values, representing the probability distribution with which an impacting particle of a given size would encounter a given local carbide coverage. Unlike Method 1 and Method 2, this approach simultaneously accounts for both the carbide area fraction and spatial distribution homogeneity, and it is inherently sensitive to the size of the impacting particle.

3. RESULTS AND DISCUSSION

3.1. Erosion test results

The erosion test results obtained for the two erodent powder grades are summarised in Table 2. Tests were conducted under equal kinetic energy conditions for the erodent particles, so that differences in erosion rate can be attributed to the interaction between particle size and substrate microstructure rather than to differences in impact energy.

Table 2
Erosion test conditions and results

Mean particle diameter [µm]	Impact velocity [m/s]	Kinetic energy [J]	ER [µg/g]
4.8 (ARD UF)	205	6×10^{-8}	48.1 ± 6.7
25.5 (ARD M)	15.9	2×10^{-7}	7.5 ± 2.2

The ARD UF powder (mean diameter 4.8 µm) produced an ER approximately six times higher than that obtained with ARD M (mean diameter 25.5 µm), despite the two conditions being designed to deliver equal kinetic energy to the substrate. This result clearly demonstrates that particle size plays a dominant role in determining erosion severity, independently of the impact energy. The underlying mechanism is related to the interaction between particle size and substrate microstructure: when the mean particle diameter is smaller than the typical inter-carbide spacing, particles preferentially impact the metallic matrix, which offers significantly lower resistance to erosion than the hard carbide phase. Conversely, when the mean particle diameter is comparable to or larger than the inter-carbide spacing, the probability that an impacting particle encounters a carbide increases substantially, and the carbides act as an effective barrier against material removal. SEM analysis of the eroded surfaces confirms this interpretation. Surfaces eroded by ARD UF show extensive and relatively uniform matrix removal with limited carbide involvement, consistent with a regime in which the matrix is the primary target of erosion. Surfaces eroded by ARD M show a qualitatively different damage pattern, with evidence of carbide-particle interactions and reduced matrix exposure, consistent with a regime in which carbides provide effective shielding of the underlying matrix (Fig. 1).

3.2. Method 1 results – carbide volume fraction

The CVF values computed for each of the six ROIs, averaged across all ten samples, are reported in Figure 4. The mean CVF across all ROIs is approximately 25%, with individual ROI values ranging from approximately 20% to 28%. The variability within each ROI, as shown by the error bars in Figure 2, reflects the inherent microstructural inhomogeneity of the hardfacing deposit, a well-known consequence of the solidification conditions during welding. While CVF provides a useful first-order descriptor of carbide content, it has a fundamental limitation as a predictor of erosion resistance: two microstructures with identical CVF values can exhibit very different spatial distributions of carbides and, consequently, very different local erosion behaviours. A microstructure in which carbides are clustered in certain regions leaves large matrix areas exposed to erodent impact, whereas a microstructure with uniformly distributed carbides of the same total area fraction provides more consistent protection. This limitation motivates the development of the complementary methods presented in Sections 3.3 and 3.4.

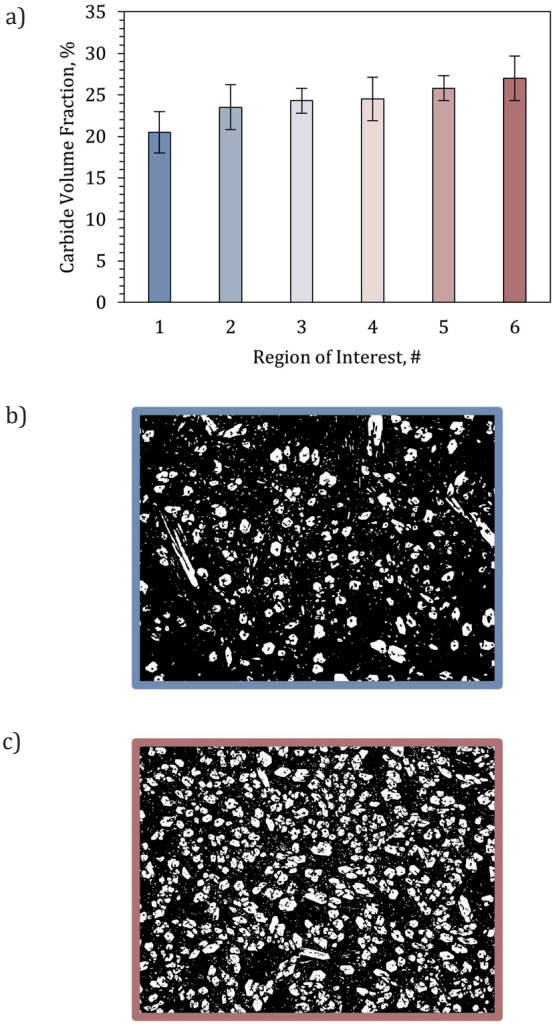

Fig. 4. Carbide volume fraction (CVF) values for each region of interest (ROI), averaged across all ten samples (a); error bars represent the standard deviation; representative optical micrograph of ROI 1, characterised by coarse, elongated primary carbides (a); representative optical micrograph of ROI 6, characterised by finer and more uniformly distributed equiaxed primary carbides (b)

3.3. Method 2 results – minimum inter-carbide distances

The distributions of minimum edge-to-edge distances between adjacent carbides, computed via Delaunay triangulation, are shown as boxplot diagrams for each ROI in Figure 5.

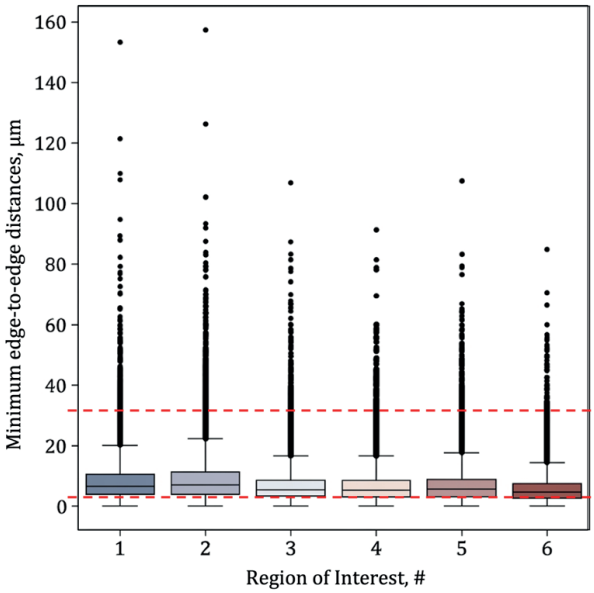

Fig. 5. Boxplot diagrams of minimum edge-to-edge distances between adjacent carbides for each region of interest (ROI). Dashed red lines indicate the mean diameters of the two erodent powders: ARD UF (d_mean = 4.8 µm) and ARD M (d_mean = 25.5 µm)

The distributions are consistently right-skewed across all ROIs, with median values below 10 µm and first quartile values close to or below 5 µm, while the third quartile remains below 25 µm in all cases. Outlier distances exceeding 60–160 µm are present in all ROIs, reflecting the occasional occurrence of large carbide-free matrix zones. The two erodent particle sizes selected for the erosion tests, 4.8 µm and 25.5 µm, are indicated as reference lines in Figure 5. Their relationship with the inter-carbide distance distributions provides a physical interpretation of the erosion results: the mean diameter of ARD UF (4.8 µm) falls below the first quartile of the distance distribution in all ROIs, meaning that the majority of inter-carbide gaps are wider than the impacting particles. Under these conditions, particles can penetrate between carbides and impact the matrix directly, resulting in high erosion rates. The mean diameter of ARD M (25.5 µm) falls near or above the third quartile in most ROIs, meaning that most inter-carbide gaps are narrower than the impacting particles, which therefore interact predominantly with the carbide phase and experience significantly lower erosion. Comparison of ROIs 1 and 2 with ROIs 3 through 6 reveals a higher dispersion of inter-carbide distances in the former, associated with the presence of coarse, elongated carbides interspersed with large carbide-free matrix regions. ROIs 3 through 6, characterised by finer, more equiaxed carbides, exhibit tighter distance distributions with lower median values and fewer extreme outliers. This result demonstrates that Method 2 is sensitive to microstructural inhomogeneity and can

identify zones of the deposit that are more vulnerable to erodent penetration between carbides. However, Method 2 presents an intrinsic limitation: it characterises only the spatial distribution of carbides without accounting for their area fraction. Two microstructures with identical inter-carbide distance distributions but different CVF values would be indistinguishable by this method alone. Furthermore, the method does not directly incorporate the geometry of the impacting particle, as it reduces the particle to a point interacting with the inter-carbide space rather than to a finite-area object interacting with a local region of the microstructure. These limitations are addressed by Method 3.

3.4. Method 3 results – moving scanning area

The frequency histograms of the coverage ratio (*Rc*) obtained by the moving scanning area method for ROI 1 and ROI 6, computed using three equivalent particle diameters (5 μm, 10 μm, and 25 μm), are shown in Figure 6. The histograms reveal two qualitatively distinct behaviours depending on the particle size and microstructural zone. For small particle diameters (*Deq* = 5 μm), the *Rc* distributions of both ROIs show a pronounced peak at *Rc* = 0, indicating that a significant fraction of possible impact positions corresponds to areas with no carbide coverage whatsoever. For ROI 1, which is characterised by coarse elongated carbides dispersed in a largely uncovered matrix, this peak reaches approximately 35%, meaning that more than one-third of potential impact positions would result in the particle striking pure matrix. For ROI 6, characterised by finer and more homogeneously distributed equiaxed carbides, the same peak is reduced to approximately 12%, reflecting a substantially lower probability of matrix-only impact. This difference directly explains the high erosion rate observed with ARD UF: under conditions where most particles impact the uncovered matrix, material removal is rapid and severe. As the particle diameter increases to *Deq* = 25 μm, the *Rc* distributions shift markedly. The peak at *Rc* = 0 disappears in both ROIs, and the distributions become centred around the mean CVF value of the analysed area (approximately 12–25% depending on the ROI), reflecting the fact that larger particles necessarily average over a wider area of the microstructure and are therefore less sensitive to local carbide-free zones. This result is consistent with the low erosion rate observed with ARD M: larger particles encounter a mixed carbide-matrix surface regardless of impact position, and the carbides provide effective resistance.

The comparison between ROI 1 and ROI 6 at all particle sizes confirms that Method 3 is sensitive to both the carbide area fraction and spatial distribution homogeneity simultaneously. ROI 6 consistently shows *Rc* distributions shifted towards higher coverage values and with a lower probability of zero-coverage impacts, reflecting its more homogeneous microstructure. This result has a direct practical implication: for a given CVF, a more homogeneous carbide distribution provides better erosion protection, particularly against fine erodent particles. Taken together, the three methods provide a hierarchical and complementary description of the microstructure. Method 1 (CVF) offers a rapid global estimate of the carbide content but cannot distinguish between homogeneous and inhomogeneous distributions. Method 2 characterises the spatial distribution through inter-carbide distances and enables direct identification of critical particle size thresholds, but does not account for the carbide area fraction or particle geometry. Method 3 integrates both coverage and spatial homogeneity into a single particle-size-dependent statistical descriptor, at the cost of higher computational demand. For practical applications, Method 2 is recommended as a rapid screening tool, while Method 3 is recommended for detailed statistical characterisation when the erodent particle size distribution is known.

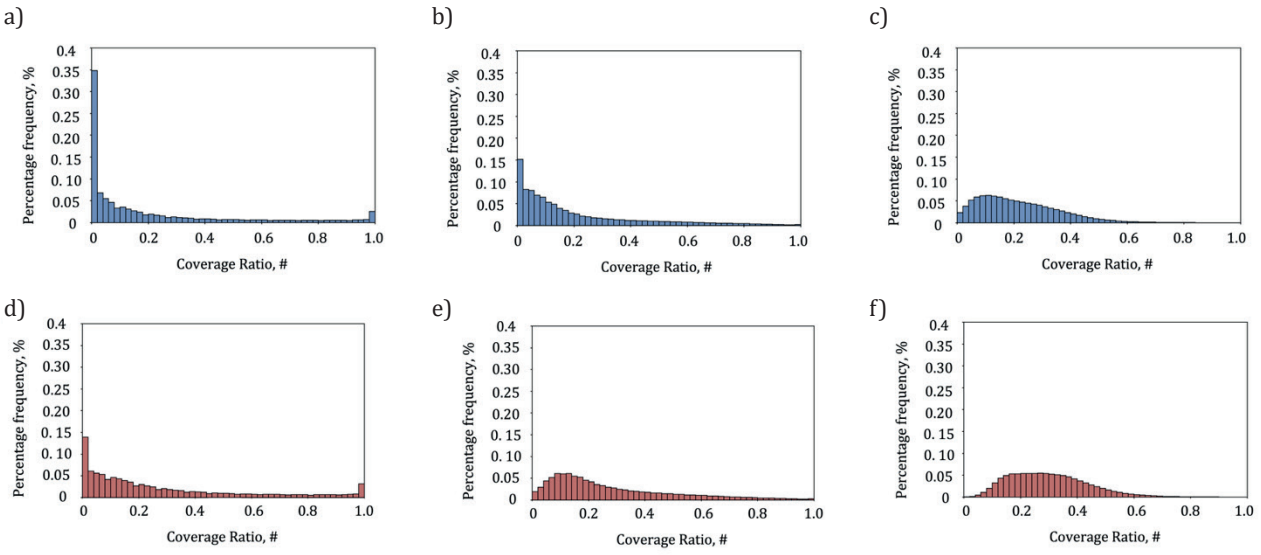

Fig. 6. Percentage frequency histograms of the coverage ratio (*Rc*) obtained by the moving scanning area method for two representative ROIs: a) ROI 1, *Deq* = 5 μm; b) ROI 1, *Deq* = 10 μm; c) ROI 1, *Deq* = 25 μm; d) ROI 6, *Deq* = 5 μm; e) ROI 6, *Deq* = 10 μm; f) ROI 6, *Deq* = 25 μm. ROI 1 is characterised by coarse elongated carbides, ROI 6 by finer and more homogeneously distributed equiaxed carbides

The proposed digital image processing framework is not intrinsically limited to high-chromium cast irons, since it relies on a general microstructural descriptor: the spatial distribution and area coverage of erosion-resistant hard phases within a softer matrix. In principle, the same approach could be extended to other two-phase or particle-reinforced systems, including hypereutectic cast irons, Ni-hard alloys, metal matrix composites, and thermally sprayed coatings, provided that the phases can be segmented reliably. Nevertheless, extrapolation to other systems must be treated with caution.

The predictive relevance of the extracted descriptors depends on whether the controlling erosion mechanisms are governed by the same length-scale relationship between the erodent size, hard-phase spacing, and matrix exposure. Therefore, any extension of the method should include material-specific validation, especially when the morphology, connectivity, toughness, or bonding of the hard phase differs from that of carbides in high-chromium cast irons. In this context, the ratio between the erodent particle size and characteristic microstructural spacing is likely to be a key scaling parameter.

4. CONCLUSIONS

This study investigated the erosive wear resistance of a Fe-Cr-C high chromium cast iron hardfacing alloy through solid particle erosion tests and three digital image processing methods to quantitatively characterise the primary M_7C_3 carbide microstructure. The following conclusions can be drawn:

- The ER decreased significantly with the increasing erodent particle size under equal kinetic energy conditions, with ARD UF (mean diameter 4.8 μm) producing an ER approximately six times higher than ARD M (mean diameter 25.5 μm). This indicates that the ratio of the erodent particle size to the microstructural inter-carbide spacing is a governing parameter of erosion severity, independent of the impact energy.
- The carbide volume fraction (Method 1), while widely used in the literature as a descriptor of HCCI wear resistance, proved insufficient as a standalone predictor of erosion behaviour. It provides no information on the spatial distribution of carbides and cannot distinguish between microstructures with homogeneous and inhomogeneous carbide arrangements that may exhibit substantially different erosion resistances.
- The minimum inter-carbide distance method based on Delaunay triangulation (Method 2) enabled quantitative characterisation of carbide spatial distribution and direct identification of critical erodent particle size thresholds relative to the inter-carbide spacing distribution. ROIs characterised by coarse, elongated carbides showed wider and more dispersed inter-carbide distance distributions, indicating greater vulnerability to fine erodent penetration between carbides. This method is an efficient preliminary screening tool due to its relatively low computational demand.
- The moving scanning area method (Method 3) provided the most complete microstructural descriptor by simultaneously accounting for the carbide area fraction and spatial distribution homogeneity as a function of erodent particle size. The frequency histograms of the coverage ratio showed that microstructural zones with finer, more homogeneously distributed carbides exhibit a significantly lower probability of zero-coverage impacts, particularly for small erodent particles, directly explaining the higher erosion severity observed with ARD UF. This method is recommended for detailed statistical characterisation when the erodent particle size distribution is known, despite its higher computational cost.

The results demonstrate that carbide distribution homogeneity is a critical parameter governing erosion resistance in HCCIs and that its quantitative assessment requires descriptors beyond CVF. The image analysis framework proposed in this study provides a physically grounded statistical tool for correlating microstructure and erosion resistance in hardfacing alloys.

ACKNOWLEDGEMENTS

The authors wish to thank Eng. Andrea Cordone and Eng. Lorenzo Colombani for their support during the experimental erosion tests, and Stephan Gazzini for developing the Python image analysis code.

REFERENCES

[1] Tandon D., Li H., Pan Z., Yu D. & Pang W. (2023). A review on hardfacing, process variables, challenges, and future works. *Metals*, 13(9), 1512. DOI: https://doi.org/10.3390/met13091512.

[2] Badisch E. & Roy M. (2013). Hardfacing for Wear, Erosion and Abrasion. In: M. Roy (Ed.), *Surface Engineering for Enhanced Performance against Wear* (pp. 149–191). Vienna: Springer. DOI: https://doi.org/10.1007/978-3-7091-0101-8.

[3] Budinski K.G. & Budinski S.T. (2021). *Tribomaterials: Properties and Selection for Friction, Wear, and Erosion Applications*. ASM International. DOI: https://doi.org/10.31399/asm.tb.tpsfwea.9781627083232.

[4] Lin C.-M., Chang C.-M., Chen J.-H., Hsieh C.-C. & Wu W. (2009). Microstructural evolution of hypoeutectic, near-eutectic, and hypereutectic high-carbon Cr-based hard-facing alloys. *Metallurgical and Materials Transactions A*, 40, 1031–1038. DOI: https://doi.org/10.1007/s11661-009-9784-6.

[5] Wiengmoon A. (2011). Carbides in high chromium cast irons. *Naresuan University Engineering Journal*, 6(1), 64–71. DOI: https://doi.org/10.14456/nuej.2011.6.

[6] Li P., Yang Y., Shen D., Gong M., Tian C. & Tong W. (2020). Mechanical behavior and microstructure of hypereutectic high chromium cast iron: the combined effects of tungsten, manganese and molybdenum additions. *Journal of Materials Research and Technology*, 9(3), 5735–5748. DOI: https://doi.org/10.1016/j.jmrt.2020.03.098.

[7] Gaqi Y., Kusumoto K., Shimizu K. & Purba R.H. (2023). Effect of carbide orientation on wear characteristics of high-alloy wear-resistant cast irons. *Lubricants*, 11(7), 272. DOI: https://doi.org/10.3390/lubricants11070272.

[8] Liu S., Zhou Y., Xing X., Wang J., Ren X. & Yang Q. (2016). Growth characteristics of primary M7C3 carbide in hypereutectic Fe-Cr-C alloy. *Scientific Reports*, 6, 32941. DOI: https://doi.org/10.1038/srep32941.

[9] Rajicic B.M., Maslarevic A., Bakic G.M., Maksimovic V. & Djukic M.B. (2023). Erosion wear behavior of high chromium cast irons. *Transactions of the Indian Institute of Metals*, 76, 1427–1437. DOI: https://doi.org/10.1007/s12666-022-02860-7.

[10] Sapate S.G. & Rama Rao A.V. (2004). Effect of carbide volume fraction on erosive wear behaviour of hardfacing cast irons. *Wear*, 256(7–8), 774–786. DOI: https://doi.org/10.1016/S0043-1648(03)00527-1.

[11] Karantzalis A.E., Lekatou A. & Diavati E. (2009). Effect of destabilization heat treatments on the microstructure of high-chromium cast iron: A microscopy examination approach. *Journal of Materials Engineering and Performance*, 18, 1078–1085. DOI: https://doi.org/10.1007/s11665-009-9353-6.

[12] Jindal C., Singh Sidhu B., Kumar P. & Singh Sidhu H. (2022). Performance of hardfaced/heat treated materials under solid particle erosion: A systematic literature review. *Materials Today: Proceedings*, 50, 629–639. DOI: https://doi.org/10.1016/j.matpr.2021.03.441.

[13] Kibble K.A. & Pearce J.T.H. (1993). Influence of heat treatment on the microstructure and hardness of 19% high-chromium cast irons. *Cast Metals*, 6(1), 9–15. DOI: https://doi.org/10.1080/09534962.1993.11819121.

[14] Tarodiya R. & Levy A. (2021). Surface erosion due to particle-surface interactions – A review. *Powder Technology*, 387, 527–559. DOI: https://doi.org/10.1016/j.powtec.2021.04.055.

[15] Lindsley B.A. & Marder A.R. (1999). The effect of velocity on the solid particle erosion rate of alloys. *Wear*, 225–229 (Part 1), 510–516. DOI: https://doi.org/10.1016/S0043-1648(99)00085-X.

[16] Oka Y.I. & Yoshida T. (2005). Practical estimation of erosion damage caused by solid particle impact. *Wear*, 259(1–6), 102–109. DOI: https://doi.org/10.1016/j.wear.2005.01.040.

[17] Sapate S.G. & RamaRao A.V. (2006). Erosive wear behaviour of weld hardfacing high chromium cast irons: effect of erodent particles. *Tribology International*, 39(3), 206–212. DOI: https://doi.org/10.1016/j.triboint.2004.10.013.

[18] ASTM International. (2013). ASTM G76-07: Standard Test Method for Conducting Erosion Tests by Solid Particle Impingement Using Gas Jets. ASTM International.

[19] Fortini A., Suman A., Vulpio A., Merlin M. & Pinelli M. (2021). Microstructural and erosive wear characteristics of a high chromium cast iron. *Coatings*, 11(5), 490. DOI: https://doi.org/10.3390/coatings11050490.

[20] Fortini A., Suman A., Zanini N. & Cruciani G. (2022). Erosive wear behavior of high-chromium cast iron: combined effect of erodent powders and destabilization heat treatments. *Coatings*, 12(8), 1218. DOI: https://doi.org/10.3390/coatings12081218.

[21] Fortini A., Suman A. & Zanini N. (2023). An experimental and numerical study of the solid particle erosion damage in an industrial cement large-sized fan. *Engineering Failure Analysis*, 146, 107058. DOI: https://doi.org/10.1016/j.engfailanal.2023.107058.

[22] ISO 12103-1:2016. (2016). Road vehicles – Test contaminants for filter evaluation – Part 1: Arizona test dust. International Organization for Standardization.

[23] Schneider C.A., Rasband W.S. & Eliceiri K.W. (2012). NIH Image to ImageJ: 25 years of image analysis. *Nature Methods*, 9, 671–675. DOI: https://doi.org/10.1038/nmeth.2089.

Journal of Casting & Materials Engineering Vol. 10 No. 2 (2026) 42–53
https://doi.org/10.7494/jcme.2026.10.2.42

Numerical Optimisation of Investment-Cast Wheel Components for Drone Applications Using MAGMASOFT®

Joshua Samuel Isaac Jonthala[a*], Janusz Lelito[b]

[a]Foundry Institute, Technische Universität Bergakademie Freiberg, Bernhard-von-Cotta-Str. 4, 09599 Freiberg, Germany
[b]AGH University of Krakow, Faculty of Foundry Engineering, 23 Reymonta St., 30 059 Krakow, Poland
[*]*e-mail: joshua-samuel-isaac.jonthala@student.tu-freiberg.de*

Received: 11 April 2026/Accepted: 26 May 2026/Published online: 18 June 2026
This article is published with open access at AGH University of Krakow Journals

Abstract

Investment casting technology of thin-walled components for drone applications requires precise filling and solidification control to minimise porosity and ensure structural integrity. Porosity is one of the most common defects found in castings, and its prediction and analysis are essential for improving the quality of complex superalloy components. In this work, porosity-related defects were examined using the MAGMASOFT® 6.1 numerical simulation software for casting, focusing on the filling and solidification behaviour of an investment casting wheel body component in drone applications. A series of simulations were performed, and two design and simulation versions were developed, analysed and compared.

The wheel body component selected for this work is made of IN713 superalloy. The numerical modelling included the assessment of porosity distribution, hot spot formation, filling behaviour, cooling, and solidification patterns. Fifteen combinations of alloy and shell initial temperatures were evaluated to determine the most favourable thermal conditions for reducing porosity, considering the specific geometry and casting characteristics of the wheel. Based on the initial results, the casting design was modified by adjusting the runner geometry and assembly configuration.

This study introduces a two-stage simulation approach to optimise porosity reduction. The second version of the simulations demonstrated a noticeable reduction in pores, particularly in critical regions of the wheel body. The findings can support drone component manufacturers in improving casting reliability. The results confirm that simulation-driven optimisation of the casting design and thermal parameters can significantly improve the quality of the components produced by investment casting technology.

Keywords:

thin-walled casting, investment casting, numerical simulation, IN713 superalloy, shrinkage porosity, solidification

1. INTRODUCTION

Investment casting, also known as lost-wax casting, is a precision manufacturing technology widely used for producing small castings and geometrically complex components with high dimensional accuracy. The investment casting process allows it to produce extremely thin wall thicknesses. The limits that are generally quoted are, for steels, a minimum wall thickness of 1.5 mm and for light alloys 1 mm, subject to design acceptability. The production of these very thin wall thicknesses is greatly assisted by the elevated initial mould temperatures during casting and, of course, by the *vacuum casting* techniques now employed on an increasing scale [1].

The process begins with the fabrication of a wax pattern that replicates the final geometry of the component. These patterns may be produced through traditional tooling or increasingly through additive manufacturing, which enables rapid prototyping and the creation of intricate internal features.

The wax assembly is repeatedly coated in a ceramic slurry and refractory material to build a robust shell capable of withstanding high casting temperatures. Automated shellbuilding systems are often employed to ensure a uniform coating thickness and consistent mechanical properties of the mould. After curing, the assembly undergoes dewaxing, typically through steam autoclaving or flashfire methods, leaving a hollow ceramic mould. Preheating the mould removes residual moisture and reduces thermal stresses during metal pouring.

Casting is performed under a vacuum to prevent oxidation and minimise gas porosity in the molten superalloy. This controlled environment is essential for producing components with the mechanical integrity required for high-temperature applications. Once the alloy solidifies, the ceramic shell is removed, and the casting undergoes finishing operations such as trimming, machining, and heat treatment. Post-cast heat treatments are critical for nickel-based superalloys, as they promote microstructural homogenisation and enhance creep resistance, strength, and oxidation performance [2]. The main stages of the investment casting process are illustrated in Figure 1.

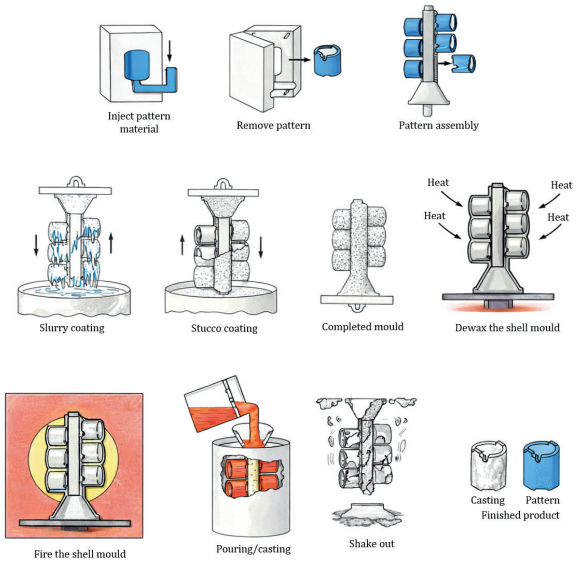

Fig. 1. Basic steps involved in investment casting [3]

Nickel-based superalloys such as IN713 are widely used in high-temperature aerospace components because of their excellent strength, corrosion resistance, and thermal stability [4, 5]. Like other cast Ni-base alloys, IN713 derives its mechanical performance from a γ/γ′ microstructure, where the γ′ (Ni_3(Al, Ti)-based phase provides high strength at elevated temperatures. Sims' foundational work established the importance of γ′ strengthening and solid-solution elements in defining the creep and oxidation resistance of cast superalloys, including IN713 [4].

Recent studies on IN713C confirm these microstructural–mechanical property relationships. Moreira et al. reported that as-cast IN713C exhibits a dendritic solidification structure with inter-dendritic segregation and carbide formation, features that strongly influence tensile strength, hardness, and high-temperature performance [6]. These microstructural characteristics are typical of cast Ni-based superalloys and highlight the sensitivity of IN713C to solidification conditions. The typical microstructure of as-cast IN713C is depicted in Figure 2.

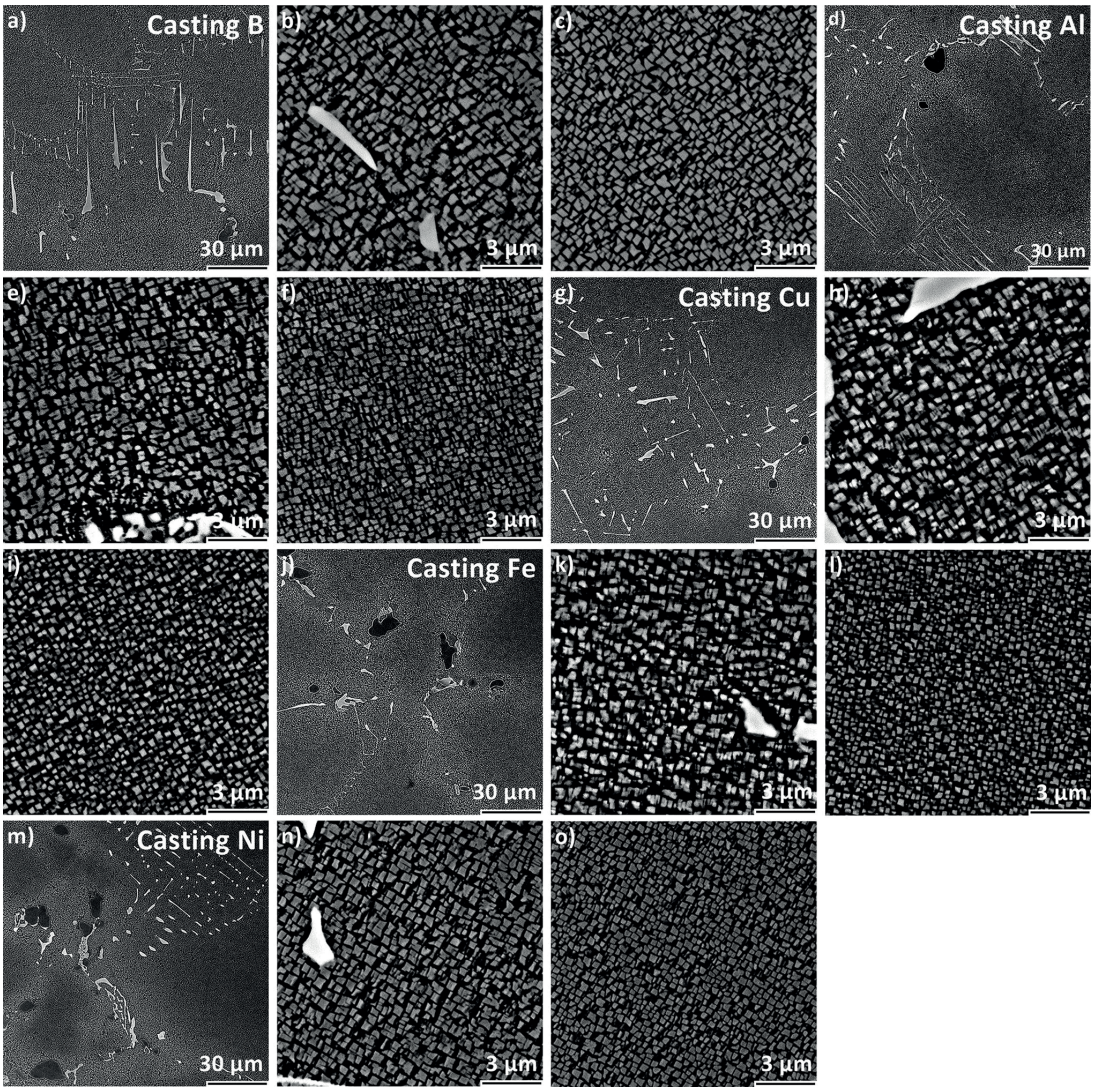

Fig. 2. Microstructure of Inconel 713C castings: (a, d, g, j, m) inter-dendritic spaces; (b, e, h, k, n) γ′ in inter-dendritic space; (c, f, i, l, o) γ′ precipitates in dendrite arm [7]

In investment casting, IN713 benefits from the ability to form complex geometries but remains sensitive to shrinkage porosity and segregation due to its high γ′ content and solidification temperature. Achieving optimal mechanical performance therefore depends on controlled solidification and appropriate ceramic shell systems. The chemical composition of the IN713 alloy used in this study is presented in Table 1.

Table 1
Chemical composition of alloy IN713 [7]

Element	Typical content [%]	Function in alloy
Nickel (Ni)	~74	Base element
Chromium (Cr)	12–14	Oxidation and corrosion resistance
Molybdenum (Mo)	4–5	Solidsolution strengthening
Aluminium (Al)	5.5–6.5	γ′ (Ni_3Al,) formation for precipitation hardening
Titanium (Ti)	0.5–1.0	Additional γ′ strengthening
Carbon (C)	0.08–0.16	Carbide formation for creep resistance
Boron (B)	0.008–0.020	Grainboundary strengthening

High- or medium-density alumina (Al_2O_3) ceramic shells are widely used in investment casting because of their excellent thermal stability and chemical inertness at the high temperatures required for processing nickel-based superalloys. Alumina shells exhibit low reactivity with molten alloys, which helps minimise interfacial reactions and surface defects during casting. Varfolomeev and Shcherbakova demonstrated that Al_2O_3–Al_2O_3 shell systems maintain good chemical compatibility with nickel-based superalloys, reducing the formation of reaction layers at the mould-metal interface and improving the surface quality of the final casting [8].

The performance of alumina shells depends strongly on their density, slurry formulation, and stucco selection. Optimising these parameters enhances shell strength, permeability, and thermal shock resistance; properties essential for preventing cracking during dewaxing and metal pouring. Dave and Kaila emphasised that careful selection and optimisation of ceramic shell materials, including alumina-based systems, significantly improves mould integrity and casting reliability in industrial investment-casting operations [9].

Simulation is the imitation of the operation of a real-world process or system over time. Whether done by hand or on a computer, simulation involves the generation of an artificial history of a system and the observation of that artificial history to draw inferences concerning the operating characteristics of the real system that is represented [10]. In modern foundry practice, casting simulation has become an essential tool, enabling virtual prototyping of mould filling, solidification, defect prediction, etc. This significantly reduces development time and cost by minimising trial-and-error iterations and improving process reliability. Numerous studies have shown that simulation helps identify potential defects such as shrinkage porosity, misruns, or hot spots before physical production, thereby improving casting quality and increasing yield [3, 11–13]. The general workflow of the casting simulation process implemented in MAGMASOFT® is illustrated in Figure 3.

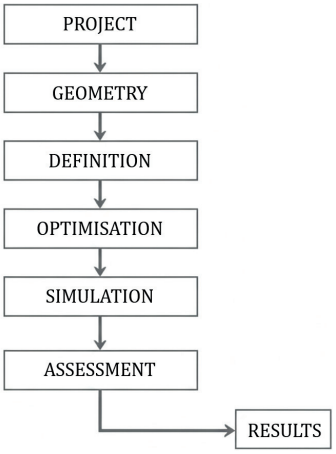

Fig. 3. MAGMASOFT® casting simulation process flow chart

For this study, the investment-casting simulations were performed using MAGMASOFT®, a commercial casting-process simulation piece of software widely used in industry and research. The numerical calculations were carried out at the Faculty of Foundry Engineering at AGH University of Krakow. MAGMASOFT® includes a dedicated Investment Casting module that models mould filling, solidification, defect (porosity) prediction, etc. The software employs a Finite Volume Method (FVM) to discretise the computational domain and solve the governing heat-transfer and fluid-flow equations.

Accurate numerical modelling requires the definition of uniqueness conditions:

- geometric conditions: describing the shape, dimensions, and topology of the casting, shell, and gating system;
- physical conditions: specifying thermophysical and physicochemical properties of alloys and ceramic materials;
- initial conditions: defining the temperature distribution and state of the system at the start of filling values;
- boundary conditions: describing interactions between casting, mould, and environment, including heat-transfer coefficients, inlet, hot topping, sand permeability, convection, and radiation.

These conditions collectively determine the fidelity of the simulation and its ability to predict real casting behaviour during solidification. As highlighted by Sabau and others, the accuracy of investmentcasting simulation depends strongly on the correct representation of interfacial heat transfer, mould properties, and radiative heat exchange [14].

The cooling of an investment casting is governed primarily by the total heat loss from the ceramic shell through thermal radiation and convection. Because investment cast components often have large, complex surface areas, accurately resolving radiative exchange across the entire shell can be computationally expensive. To address this, commercial simulation tools such as MAGMASOFT® implement specialised radiation

algorithms that reduce computation time while maintaining acceptable accuracy for industrial casting simulations [15].

Thermal convection refers to the transport of heat within fluids (liquids and gases) that involves not only the transfer of energy but also the movement of the material itself and its accompanying heat content. This convection becomes relevant to investment casting when cooling media such as air circulate around the mould to extract heat from the system.

There are two types of convection:

1) forced convection: driven by external means such as fans or directed airflow, enhancing heat removal from the mould surface;
2) natural (free) convection: driven by buoyancy forces caused by temperature-induced density differences in the surrounding air.

The convective heat flux is described by *Newton's Law of Cooling* [16]**:**

$$q = -hA(T_s - T_f) \tag{1}$$

where:

q – heat flux [W] perpendicular to the surface area A [m^2],
h – convection heat transfer coefficient [W/(m^2 · K)],
T_s – surface temperature of the casting or mould [K],
T_f – temperature of the cooling fluid [K].

Thermal radiation: Thermal radiation is the transfer of energy by electromagnetic waves and does not require a medium, making it especially important in high-temperature or vacuum investment-casting environments. During the early stages of cooling and solidification, radiative heat transfer often dominates because ceramic shells have high emissivity and molten metals radiate strongly at elevated temperatures.

The radiative heat transfer rate is described by the *Stefan–Boltzmann Law* [16]. In the present study, emissivity is included implicitly through the material properties defined in the MAGMASOFT® database; therefore, it is not explicitly varied in the analytical formulation.

$$q = \varepsilon\sigma A T^4 \tag{2}$$

where:

q – radiative heat transfer rate [W],
ε – emissivity of the material [–] (for a black body ε = 1, while for real materials ε < 1),
σ – Stefan-Boltzmann constant [5.669 · 10^{-8} W/ (m^2 · K^4)],
A – radiating surface area [m^2],
T – absolute temperature [K].

In the present work, a constant metal–mould interfacial heat transfer coefficient (HTC) was applied at the casting–shell interface [16]:

$$h = \frac{q}{T_s - T_a} \tag{3}$$

where:

h – heat transfer coefficient [W/ (m^2 · K)],
q – amount of heat transfer [W/m^2],
T_s – surface temperature [K],
T_a – temperature of the surrounding fluid [K].

This value represents a typical order of magnitude for good metal-ceramic contact during the early stages of solidification. However, it does not account for the time-dependent decrease in HTC associated with gap formation and mould expansion, as discussed by Sabau in numerical studies of investment casting. Consequently, the predicted cooling rates and solidification times should be interpreted as an approximation rather than an exact reproduction of experimental conditions [14].

2. MATERIALS AND METHODS

2.1. Component geometry and initial design

The component analysed in this study is a wheel body intended for drone propulsion systems. The geometry was created in SOLIDWORKS, incorporating thin blades and a central hub to replicate the aerodynamic and structural requirements of drone applications. A straight central runner was designed and connected to the wheel body to form the initial casting configuration (Figs. 4 and 5).

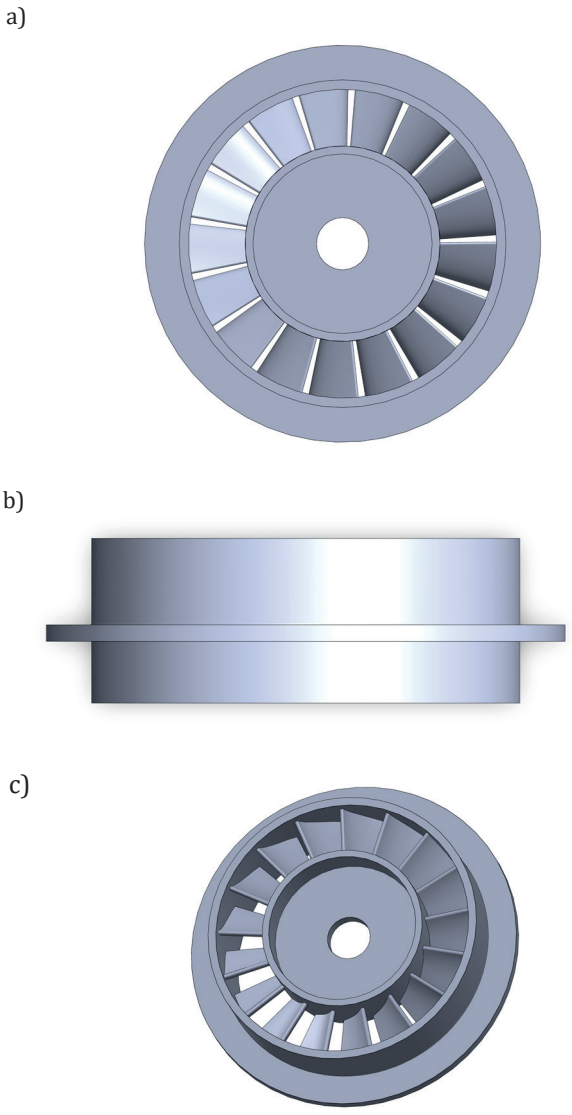

Fig. 4. CAD model of the investment-cast wheel component developed in SOLIDWORKS: a) top view; b) front view; c) isometric view

For investment casting, the wheel was assembled into a single-part tree structure. The complete geometry was exported as an STL file and imported into MAGMASOFT® for numerical simulation. Within the simulation environment, a pouring basin and hot topping were added, and material assignments were defined for the alloy, ceramic shell, and feeding system (Figs. 5 and 6).

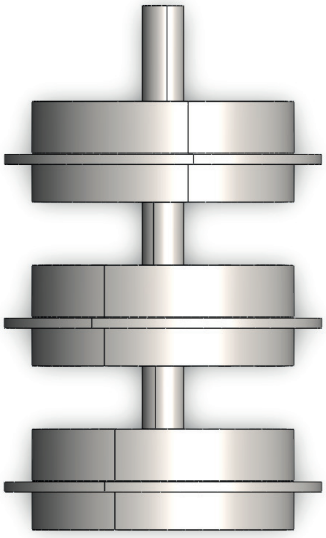

Fig. 5. Assembly of the investment-cast wheel component in SOLIDWORKS

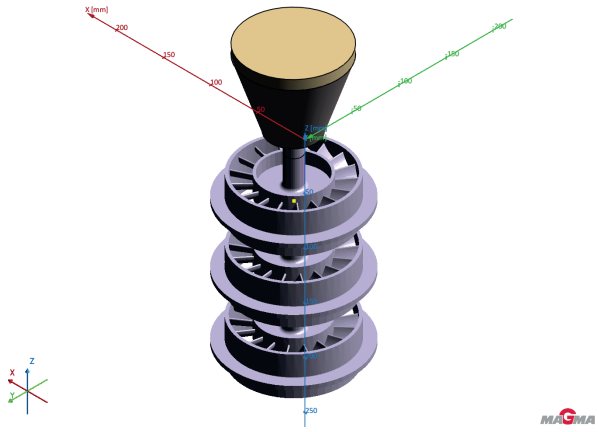

Fig. 6. Pouring basin and hot-topping geometry generated in the MAGMASOFT® geometry module

2.2. Mesh generation

Accurately predicting hot spot and porosity formation requires a fine mesh resolution in thin-walled regions. MAGMASOFT®'s advanced meshing tool was used to apply local refinement to the wheel blades and hub while maintaining coarser elements in non-critical regions. The Finite Volume Method (FVM) is used for calculations in MAGMASOFT®. A shell thickness of 10 mm is automatically generated around the casting and gating system components in mesh generation. The casting was meshed using the advanced module, while the gating system used the standard module (Fig. 7). The characteristics of the generated mesh for the initial configuration are summarised in Table 2. This ensured a good-quality mesh suitable for casting numerical simulation.

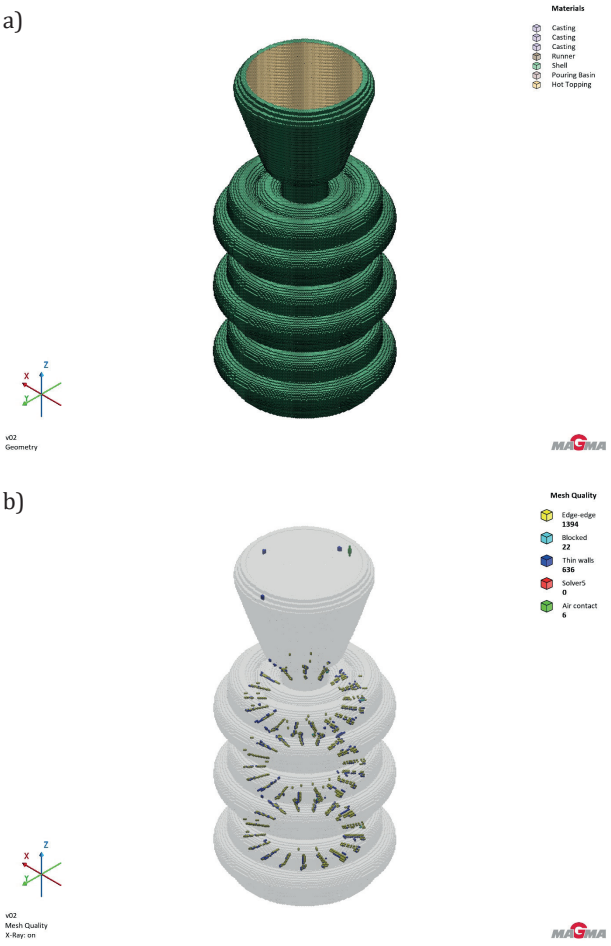

Fig. 7. Mesh generated for the casting, gating system, and ceramic shell in MAGMASOFT®: a) overall mesh distribution showing refinement in thin-walled regions of the wheel; b) detailed view highlighting element density and mesh quality in critical areas

Table 2
Mesh elements of initial design

Edge-to-edge elements	1394
Thin-wall elements	636
Blocked elements	22
Solver-critical elements	0
Air contact elements	6

2.3. Material definitions and boundary conditions

The casting alloy selected for the study was IN713, a nickel-based superalloy commonly used in high-temperature rotating components. The ceramic shell was modelled using the standard shell alumina high density material available in MAGMASOFT® database, with constant heat transfer coefficients applied at the metal-mould interface (Table 3).

Table 3
Simulation parameters considered

Alloy pouring temperature	1450–1550°C
Pouring time	Automatic filling control
Shell preheat temperature	800–1000°C
Temperature step	50°C
Feeding effectivity	50%
Sand (shell) permeability	300 cm^3/min
Hot topping initial temperature	20°C
Heat transfer coefficient (HTC)	1000 $W \cdot m^{-2} \cdot K^{-1}$

A shell permeability of 300 cm^3/min was selected to represent the permeability conditions typical of dense alumina-based ceramic shells used in vacuum investment casting. Permeability in this range restricts gas flow through the mould wall, which is consistent with the reduced-pressure environment of vacuum processing and supports stable solidification by minimising gas entrapment. In MAGMASOFT®, this parameter influences the mould venting behaviour, thermal response, and porosity prediction, making it an essential input for accurately modelling vacuum investment-casting conditions.

These values were selected based on the literature to reflect near-realistic industrial conditions for investment casting of nickel superalloys [11, 14]. In particular, the selected alloy and shell temperatures correspond to casting conditions [2, 7], while the applied HTC values are consistent with the values used in the numerical simulations [14, 16].

2.4. Design of experiments (DOE) and optimisation in MAGMASOFT®

A total of 15 simulation variants were generated by combining the alloy initial temperatures with the shell initial temperatures, as summarised in Table 4.

Table 4
Temperature design of cast and shell

Design	Cast alloy – initial temperature [°C]	Shell – initial temperature [°C]
Design 1	1450.0	800.0
Design 2	1500.0	800.0
Design 3	1550.0	800.0
Design 4	1450.0	850.0
Design 5	1500.0	850.0
Design 6	1550.0	850.0
Design 7	1450.0	900.0
Design 8	1500.0	900.0
Design 9	1550.0	900.0
Design 10	1450.0	950.0
Design 11	1500.0	950.0
Design 12	1550.0	950.0
Design 13	1450.0	1000.0
Design 14	1500.0	1000.0
Design 15	1550.0	1000.0

Each design was evaluated for:
- porosity distribution,
- hot spot formation,
- fraction liquid evolution,
- filling behaviour and flow of molten metal.

The primary and only objective selected was to identify and minimise the porosity in the wheel body.

2.5. Redesigned geometry

Based on the findings from the initial simulation, the casting geometry was modified to improve the feeding behaviour, melt flow, and overall solidification performance. The redesign included the following changes:
- The wheel component was reshaped according to the predicted hotspot and porosity regions. A draft angle of approximately 13° was introduced and applied through a geometric extrusion in SOLIDWORKS, resulting in a more favourable solidification profile (Fig. 8).
- The runner length was increased by approximately 25% to compensate for shellthickness effects during meshing and to promote more uniform metal flow into the mould cavity (Fig. 9).
- An additional wheel was incorporated into the casting tree to increase the thermal mass of the assembly. This modification was intended to alter the solidification sequence and enhance the feeding conditions by slowing the overall cooling rate (Fig. 9).
- A new pouring basin and hottopping configuration were created using the MAGMASOFT® Geometry Module to improve melt delivery and feeding efficiency during the final stages of solidification (Fig. 10).

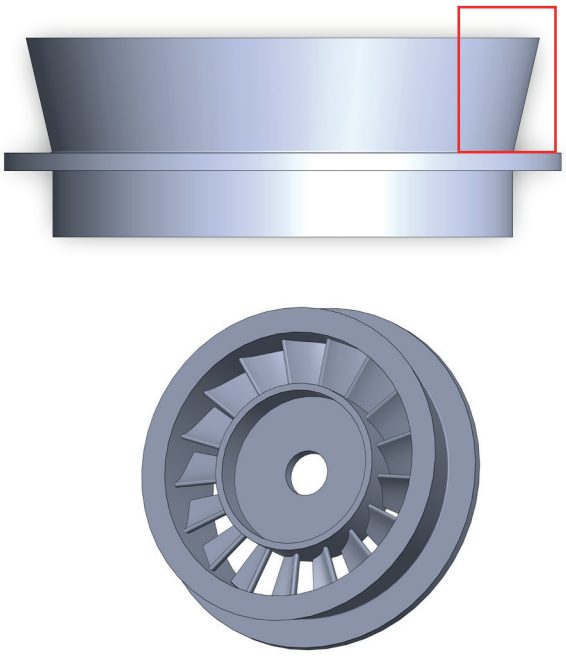

Fig. 8. Redesigned wheel geometry developed in SOLIDWORKS incorporating modifications based on initial porosity analysis

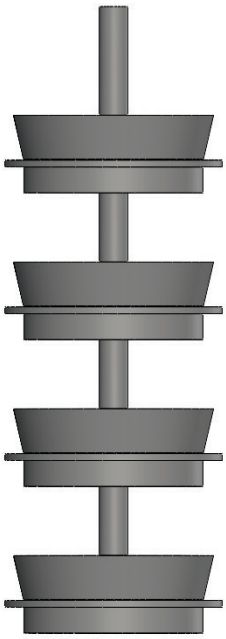

Fig. 9. Redesigned wheel geometry developed in SOLIDWORKS: assembly view showing the revised configuration of an additional wheel and extended runner prepared for numerical simulation

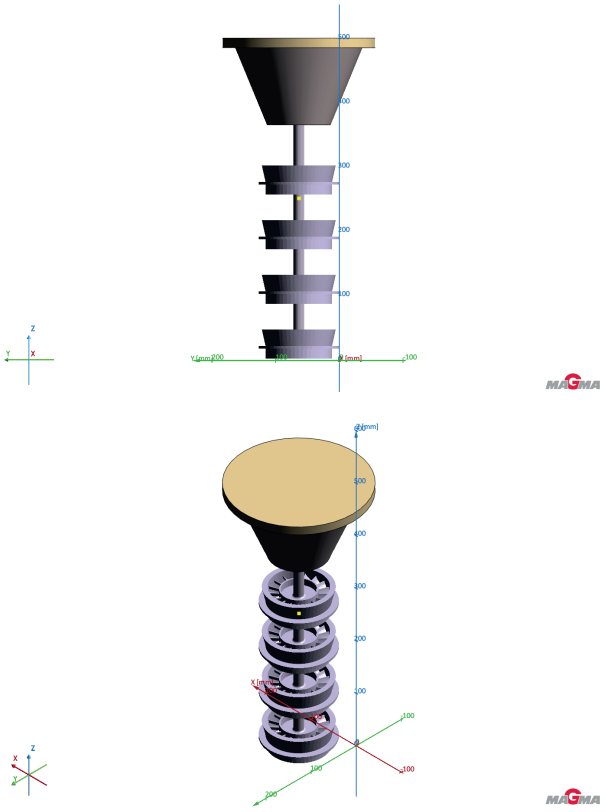

Fig. 10. Redesigned pouring basin and hot-topping configuration generated in the MAGMASOFT® Geometry Module

The redesigned model was subsequently meshed using the same refinement strategy as the baseline configuration, ensuring consistent numerical resolution across all simulations (Fig. 11). The mesh characteristics of the redesigned configuration are summarised in Table 5.

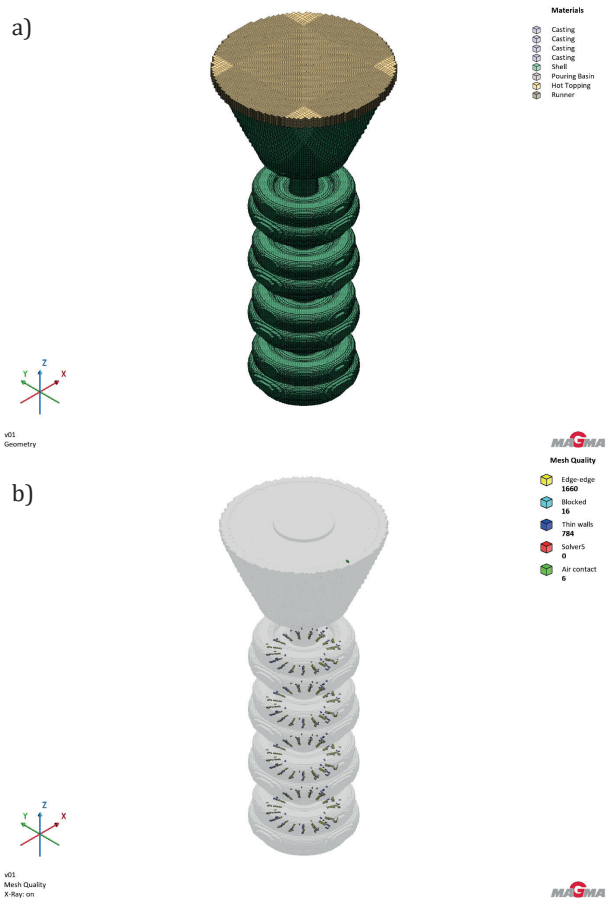

Fig. 11. Mesh generated for the redesigned casting and gating system: a) global mesh layout; b) refined mesh in thin-walled and critical areas

Table 5
Redesigned mesh elements

Edge-to-edge elements	1660
Thin-wall elements	784
Blocked elements	16
Solver-critical elements	0
Air contact elements	6

The same DOE matrix of 15 thermal variants (Table 4) was applied to the redesigned geometry.

3. RESULTS

3.1. Initial simulation results

The initial set of simulations evaluated the wheel and runner configuration under fifteen combinations of alloy and shell temperatures. The results are summarised in Table 6. The values highlighted in bold indicate the lowest porosity in the initial configuration (Design 1) and the redesigned configuration (Design 4). Among these tested variants, Design 1 (alloy initial temperature is equal 1450°C and shell is equal to 800°C) exhibited the lowest overall porosity value (5.03).

Table 6
Comparison of porosity values for initial and redesigned configurations as a function of alloy and shell temperatures

Design	Cast alloy – initial temperature [°C]	Shell – initial temperature [°C]	Porosity [–], initial design	Porosity [–], redesigned
Design 1	1450.0	800.0	**5.03**	10.36
Design 2	1500.0	800.0	5.44	11.06
Design 3	1550.0	800.0	5.55	11.85
Design 4	1450.0	850.0	5.34	**10.35**
Design 5	1500.0	850.0	5.38	11.35
Design 6	1550.0	850.0	5.52	12.22
Design 7	1450.0	900.0	5.13	10.56
Design 8	1500.0	900.0	5.50	11.46
Design 9	1550.0	900.0	5.53	12.27
Design 10	1450.0	950.0	5.16	10.76
Design 11	1500.0	950.0	5.22	11.72
Design 12	1550.0	950.0	5.58	12.08
Design 13	1450.0	1000.0	5.20	11.18
Design 14	1500.0	1000.0	5.23	11.65
Design 15	1550.0	1000.0	5.45	11.37

However, significant shrinkage porosity defects remained, concentrated in the central hub region, the blade–hub transition, and the upper parts of the wheel body. These regions correspond to thin-walled areas with restricted feeding paths, which increased their sensitivity to thermal gradients and solidification shrinkage. The observed porosity distribution is consistent with the dendritic solidification behaviour of IN713 described in the Introduction. Interdendritic regions are prone to shrinkage porosity due to solute segregation and delayed solidification, which promotes the formation of defects in the final stages of solidification. This behaviour could be correlated to the concentration of porosity in the hub and blade–hub transition regions.

The hot-spot simulation identified a dominant thermal concentration at the hub region and at the end of the blades, where solidification times exceeded approximately 230 s (Fig. 12). This prolonged local solidification promotes shrinkage porosity, most likely due to insufficient feeding and geometric constraints inherent to the initial design. The predicted hot-spot location corresponds closely with the porosity distribution obtained from the porosity-defect simulation (Fig. 13), confirming that the thermal mass of the wheel is not adequately balanced by the existing gating system. Together, these results indicate that the hub region requires improved feeding or modified geometry to mitigate shrinkage-related defects in subsequent design iterations.

The correlation analysis (Fig. 14) for the initial design reveals two distinct thermal influences on porosity formation. A strong positive correlation is observed between the initial alloy temperature and reduced porosity, indicating that higher pouring temperatures (1450–1550°C) promote improved feeding and reduced shrinkage defects. This trend reflects the longer liquidphase availability and enhanced fluidity of the melt at elevated temperatures, which support more effective inter-dendritic feeding during solidification. In contrast, the initial shell temperature exhibits a weak negative correlation with reduced porosity. Increasing the shell preheat temperature (800–1000°C) slightly increases the porosity, likely due to reduced thermal gradients and slower heat extraction, which diminish directional solidification and promote localised shrinkage.

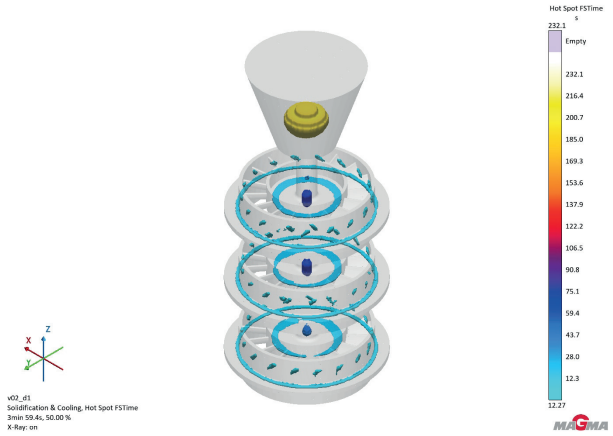

Fig. 12. Hot spot distribution for the initial design (Design 1: alloy temperature 1450°C, shell temperature 800°C)

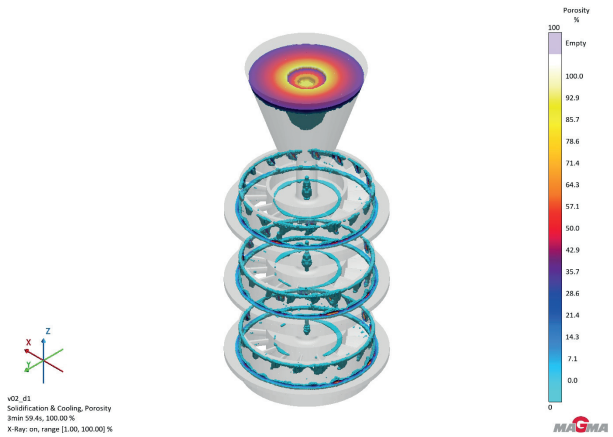

Fig. 13. Porosity distribution for the initial design (Design 1)

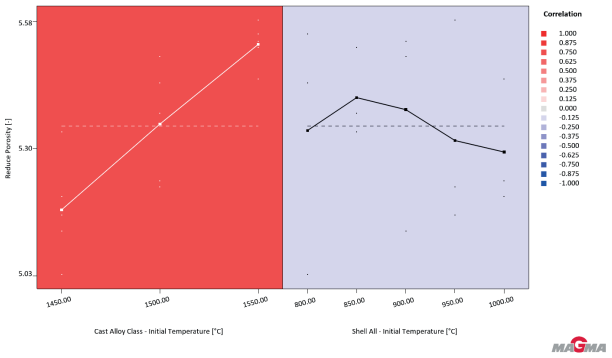

Fig. 14. Correlation of alloy and shell temperature with porosity of initial design

The pouring simulations, in contrast, revealed favourable flow conditions. Metal flow into the cavity was stable across all temperature combinations, indicating sufficient gating performance. The uniform filling suggested that the existing system could accommodate additional components on the tree, providing the idea for a redesigned geometry in the next phase of the analysis. The liquid-fraction results provided further insight into the solidification sequence (Fig. 15).

3.2. Redesigned simulation results

The redesigned configuration incorporated several geometric and gating system modifications, including a 25% longer runner, the addition of a second wheel on the casting tree, and a redesigned pouring basin with hot topping. These changes altered the thermal balance of the assembly. The extended runner improved the melt distribution towards the wheel cavity, while the additional wheel increased the overall thermal mass, slowing the cooling rate and enhancing feeding conditions during solidification.

Hot spot analysis of the redesigned configuration (Fig. 16) revealed a more uniform temperature distribution compared to the initial design, accompanied by a reduced cooling rate. The maximum solidification time increased to approximately 590 s, indicating a more controlled and progressive solidification sequence. This behaviour reflects the influence of the improved heat retention within the casting system.

The porosity distribution corresponding to the redesigned configuration (Design 4) is presented in Figure 17, with quantitative results previously summarised in Table 6. Among all simulated variants, Design 4 (alloy temperature 1450°C and shell temperature 850°C) exhibits the most favourable performance. Although the total porosity value (10.35) is higher than that of the initial configuration (5.03), a substantial reduction of porosity was achieved in critical regions, particularly in the central hub and blade-hub interface. In the redesigned configuration, porosity is predominantly located in the upper draft regions of the component, which are removed during subsequent machining operations. Therefore, despite the higher total porosity value, the redistribution of defects towards non-critical regions results in a net improvement in casting quality and structural integrity.

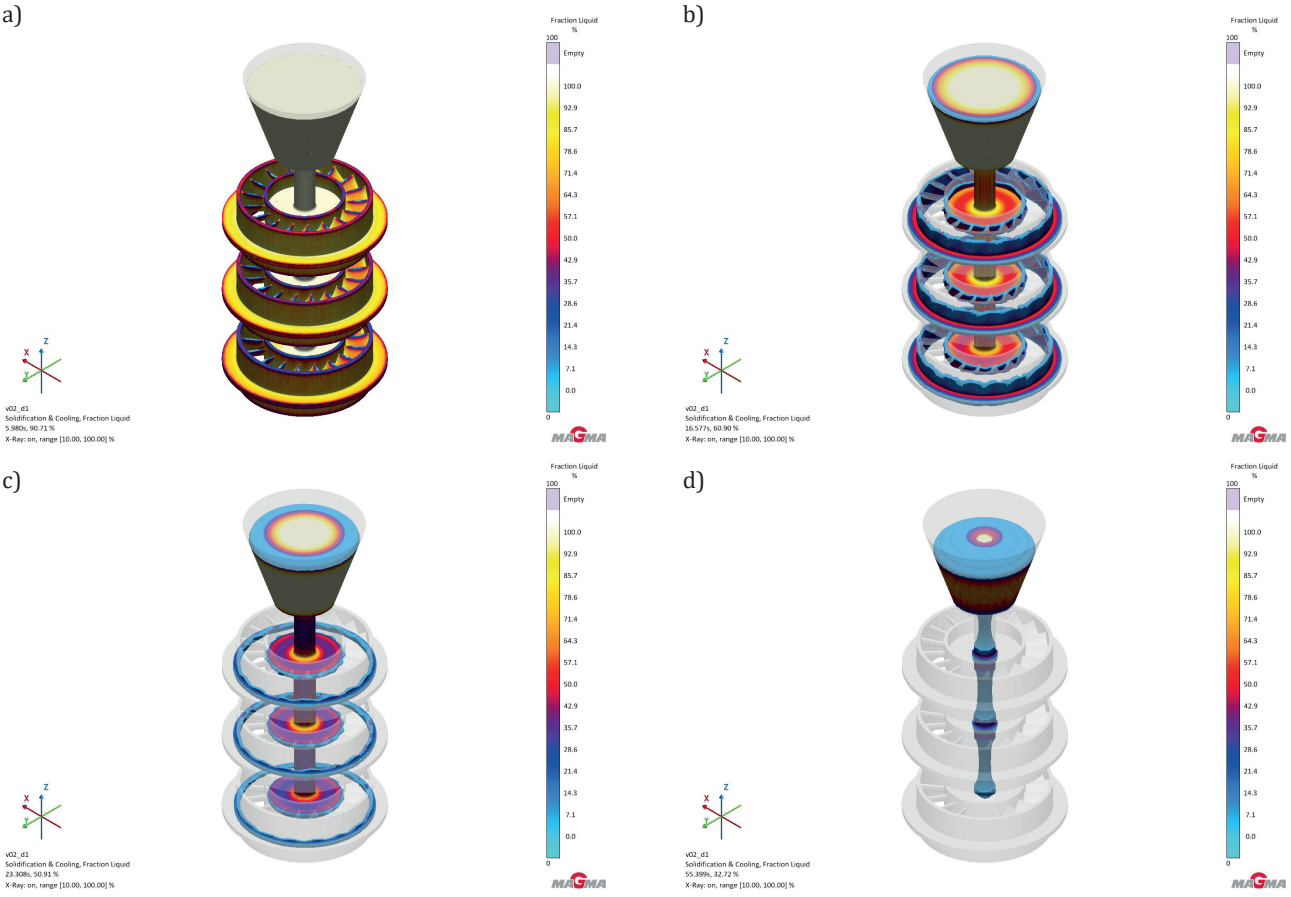

Fig. 15. Solidification stages of initial design – liquid fraction: a) 90.71%; b) 60.90%; c) 50.91%; d) 32.72%

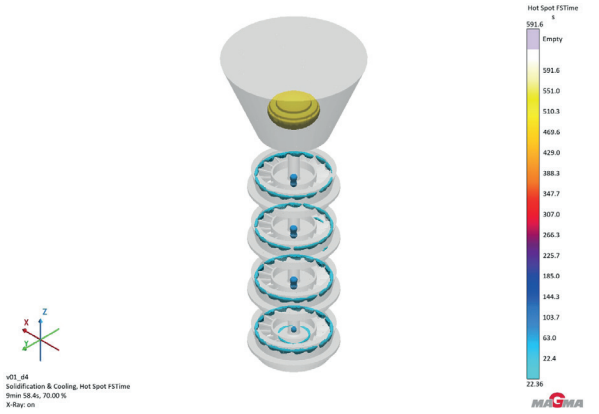

Fig. 16. Hot spot distribution for the redesigned configuration (Design 4: alloy temperature 1450°C, shell temperature 850°C)

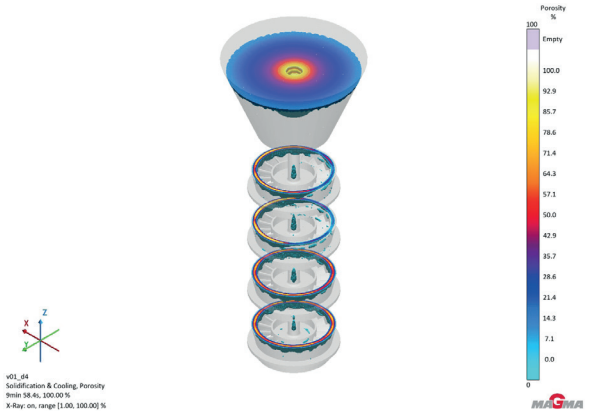

Fig. 17. Porosity distribution for the redesigned configuration (Design 4)

Correlation trends between process parameters and porosity are shown in Figure 18. Similar to the initial design, alloy superheat exhibited a strong positive influence on porosity formation, whereas shell preheating showed a weak negative influence. However, the redesigned gating system reduced the sensitivity of porosity formation to variations in shell temperature, making the alloy temperature the dominant controlling factor.

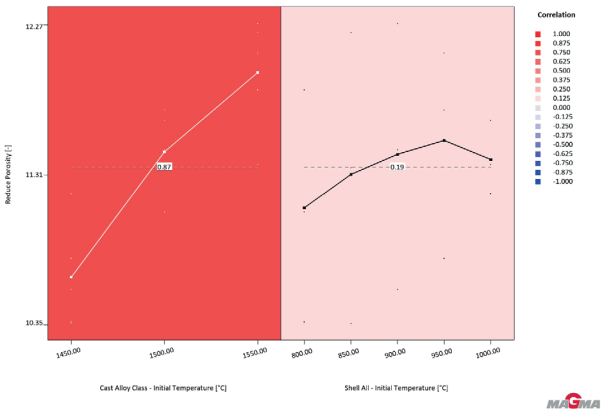

Fig. 18. Correlation of alloy and shell temperature with porosity of redesign

Further insight into the solidification behaviour is provided by the fraction liquid maps (Fig. 19), which demonstrate smoother solidification fronts and a more homogeneous temperature distribution throughout the process. The selected parameters (alloy temperature of 1450°C and shell temperature of 850°C) provided sufficient superheat to ensure complete mould filling while preventing premature solidification in thin-walled sections.

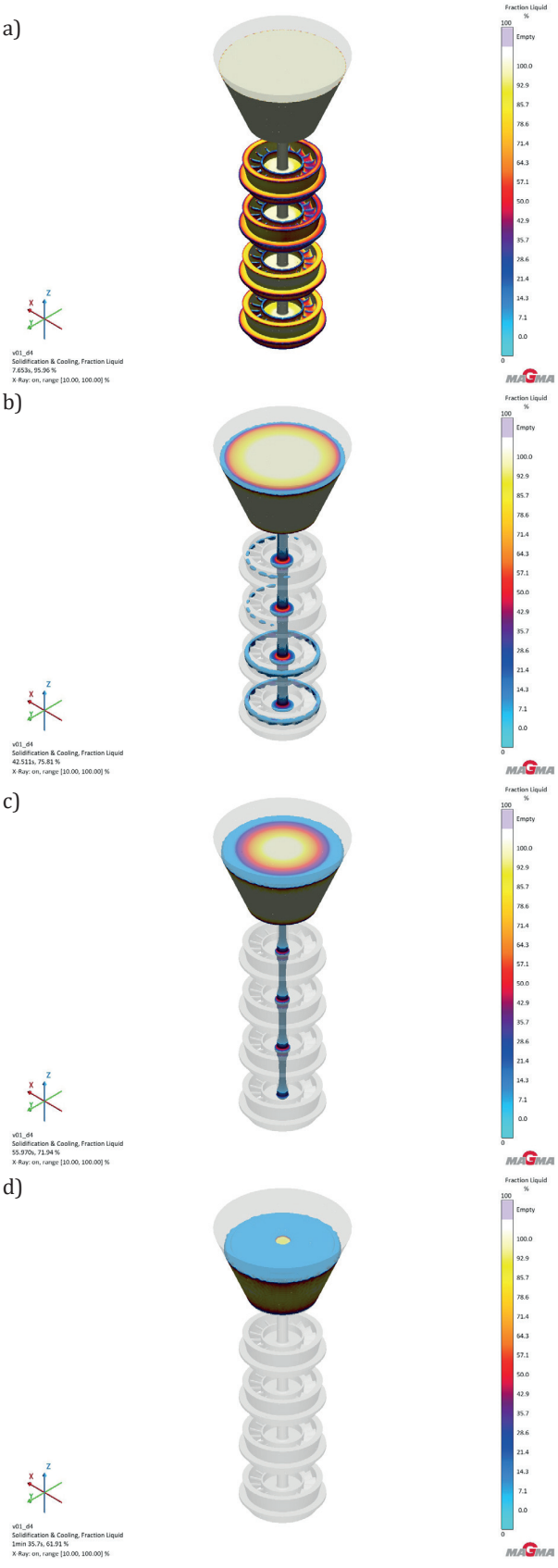

Fig. 19. Solidification stages of redesigned configuration – liquid fraction: a) 95.96%; b) 75.81%; c) 71.94%; d) 61.91%

3.3. Comparative analysis: Initial vs. redesigned

A comparison between the initial configuration (Design 1, Fig. 20) and the redesigned configuration (Design 4, Fig. 21) clearly demonstrates the benefits of the redesign. The porosity previously concentrated at the hub was significantly reduced, and shrinkage in the blade region decreased correspondingly. Although both designs maintained good filling behaviour, the redesigned configuration exhibited markedly superior feeding efficiency due to its extended solidification time and balanced thermal distribution.

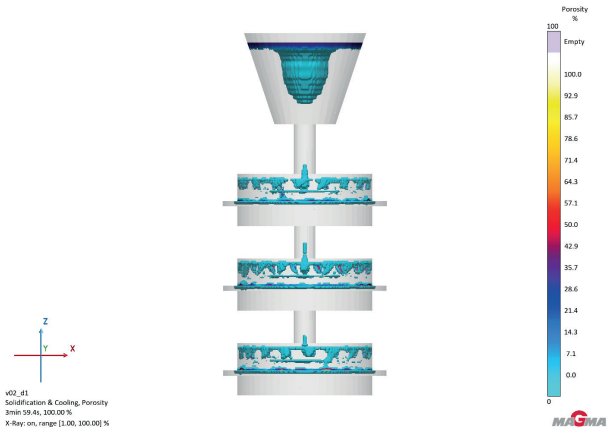

Fig. 20. Porosity distribution for the initial design (Design 1)

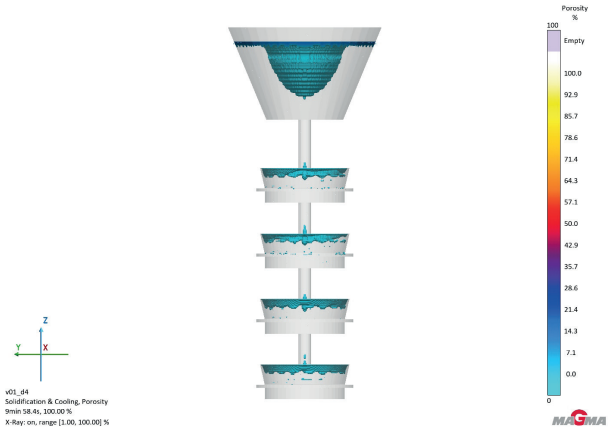

Fig. 21. Porosity distribution for the redesign (Design 4)

The hot spot duration increased from approximately 3 min 59 s in the baseline design to nearly 9 min 58 s in the optimised model, providing sufficient time for feeding and thus reducing porosity formation. Overall, the results confirm that the redesigned configuration achieved improved metallurgical soundness and thermal stability. The redesigned configuration (Design 4) effectively meets the casting quality requirements and can be further machined to restore the original geometry specifications.

4. CONCLUSIONS

The numerical simulations performed in this study demonstrated that both thermal parameters and casting system design significantly influence porosity formation in investment casting IN713 components.

In the initial configuration, the lowest porosity value (5.03) was obtained for Design 1 (1450°C alloy, 800°C shell). However, this porosity was concentrated in critical regions, particularly in the central hub and blade–hub interface, which negatively affects the structural integrity of the component.

The redesigned configuration, incorporating modifications to the runner geometry, casting tree, and pouring system, resulted in improved feeding conditions and a more favourable solidification pattern. The optimal variant was identified as Design 4 (1450°C alloy, 850°C shell), which achieved a significant porosity reduction in critical regions. Although the total porosity increased to 10.35, the defects were redistributed to non-functional regions removed during machining, resulting in improved effective casting quality.

The redesign increased the solidification time and promoted more uniform thermal gradients, enhancing feeding efficiency and reducing shrinkage porosity in critical areas. These results confirm that simulation-driven design modification is an effective approach for improving the quality and reliability of investment-cast components. The study demonstrates that optimisation of both thermal parameters and casting geometry is essential for controlling porosity formation and achieving high-quality castings for drone applications.

ACKNOWLEDGEMENTS

The work was carried out within the Erasmus+ exchange program at the AGH University of Krakow. The author would like to express their sincere gratitude to Dr hab. inż. Janusz Lelito, prof. AGH and Prof. Dr hab. Halina Krawiec of the AGH University of Krakow for accepting him into their research project and for providing access to unpublished research results.

Special thanks are extended to Prof. Dr.-Ing. Michał Szucki for his guidance and support during the specialisation in Foundry Technology and for his continued assistance.

The author would also like to thank his colleagues from the Faculty of Foundry Engineering at the AGH University of Krakow for their valuable support and insightful discussions.

REFERENCES

[1] Green Spikesley E. (1979). Investment casting. *International Journal of Materials in Engineering Applications*, 1(6), 328–334.

[2] Sjöberg G. (2010). Casting superalloys for structural applications. In: E.A. Loria (Ed.), *Superalloy 718 and Derivatives* (pp. 116–130). Warrendale: The Minerals, Metals & Materials Society.

[3] Stefanescu D.M. (2015). *Science and Engineering of Casting Solidification*. Cham: Springer.

[4] Sims C.T. (1966). A contemporary view of nickel base superalloys. *Journal of the Minerals, Metals & Materials Society*, 18(10), 1119–1130.

[5] Zýka J., Andršová I., Podhorná B. & Hrbáček K. (2014). Mechanical properties and microstructure of IN738LC nickel superalloy castings. *Materials Science Forum*, Vol. 782, 437–440. Stafa Zurich: Trans Tech Publications. DOI: https://doi.org/10.4028/www.scientific.net/MSF.782.437.

[6] Moreira M.F., Fantin L.B., Beneduce Neto F. & Azevedo C.R.F. (2021). Microstructural and mechanical characterization of as cast nickelbased superalloy IN 713C. *International Journal of Metalcasting*, 15(4), 1129–1148. DOI: https://doi.org/10.1007/s40962-020-00540-0.

[7] Rakoczy Ł., Grudzień Rakoczy M. & Cygan R. (2019). The influence of shell mold composition on the as cast macro and micro structure of thin walled IN713C superalloy castings. *Journal of Materials Engineering and Performance*, 28(7), 3974–3985. DOI: https://doi.org/10.1007/s11665-019-04098-9.

[8] Varfolomeev M.S. & Shcherbakova G.I. (2021). Interaction of a ceramic casting mold material of the Al_2O_3–Al_2O_3 composition with a nickel-based superalloy. *International Journal of Metalcasting*, 15(4), 1309–1316. DOI: https://doi.org/10.1007/s40962-020-00557-5.

[9] Dave I.B. & Kaila V.N. (2014). Optimization of ceramic shell mold materials in investment casting. *International Journal of Research in Engineering and Technology*, 3(10), 30–33. DOI: https://doi.org/10.15623/ijret.2014.0310005.

[10] Banks J. (2000). Introduction to simulation. *Proceedings of the Winter Simulation Conference*, December 10–13, Orlando, USA (pp. 9–16). Piscataway: IEEE.

[11] Campbell J. (2015). *Complete Casting Handbook: Metal Casting Processes, Metallurgy, Techniques and Design*. Oxford: Butterworth Heinemann.

[12] Socha L., Gryc K., Sviželová J., Chmiel M., Brathová M. & Filipek S. (2022). Prediction of defects of ductile iron casting by numerical simulation. *IOP Conference Series: Materials Science and Engineering*, 1243(1), 012008. DOI: https://doi.org/10.1088/1757-899X/1243/1/012008.

[13] Khan M.A.A. & Sheikh A.K. (2018). Mechanical characterization and quality of iron castings using optimized mold design: simulations and experimental validation. *The International Journal of Advanced Manufacturing Technology*, 98(1), 799–809. DOI: https://doi.org/10.1007/s00170-018-2325-y.

[14] Sabau A.S. (2005). Numerical simulation of the investment casting process. *Transactions of American Foundry Society*, 113, 407–417.

[15] MAGMA Gießereitechnologie GmbH. (2026). *MAGMASOFT®: Investment Casting Module*. Aachen: MAGMA Gießereitechnologie GmbH.

[16] Incropera F.P., DeWitt D.P., Bergman T.L. & Lavine A.S. (1996). *Fundamentals of Heat and Mass Transfer*. New York: Wiley.

Journal of Casting & Materials Engineering Vol. 10 No. 2 (2026) 54–60
https://doi.org/10.7494/jcme.2026.10.2.54

Antibacterial Polyurethane Adhesives for Medical Applications

Dominika Pitera*[a], Barbara Pilch-Pitera[b], Ireneusz Woźny[b], Dariusz Krajewski[b], Ewa Ciszkowicz[b], Karol Bester[b]

[a] The Specialist Hospital in Sanok, Autonomous Public Healthcare Centre, 26 800-lecia St., 38-500 Sanok, Poland
[b] Rzeszow University of Technology, Faculty of Chemistry, 6 Powstańców Warszawy St., 35-029 Rzeszów, Poland
e-mail: piteradominika@gmail.com

Received: 25 May 2026/Accepted: 10 June 2026/Published online: 18 June 2026
This article is published with open access at AGH University of Krakow Journals.

Abstract

In this study, polyurethane prepolymers and two-component adhesive systems with antibacterial properties were synthesised and characterised for potential biomedical applications as tissue adhesives. The developed materials were designed to operate in moist biological environments and to provide simultaneous adhesive and antibacterial functions. The viscosity of the obtained prepolymers, measured using a Brookfield viscometer, ranged from 2.30 to 3.36 Pa·s, indicating favourable rheological properties for dosing, mixing, and application on tissue surfaces. The chemical structure of the crosslinked adhesives was confirmed by FTIR spectroscopy, which revealed characteristic urethane bands and the absence of isocyanate groups, indicating complete conversion during curing. Contact angle measurements demonstrated the hydrophilic nature of the materials, suggesting good potential for adhesion to wet biological tissues. Mechanical characterisation showed medium hardness (medium-soft materials) and high adhesive strength exceeding 5 MPa, confirming suitable mechanical performance for tissue bonding applications. Antibacterial testing indicated that the incorporation of a biopolymer-based antimicrobial agent resulted in strong biocidal activity, outperforming conventional silver-based additives. The results demonstrate that the developed polyurethane-based adhesive systems combine favourable mechanical, physicochemical, and antibacterial properties, making them promising candidates for surgical applications.

Keywords:

antimicrobial activity, bio-based antimicrobial agent, montmorillonite, polylysine

1. INTRODUCTION

The development of modern biomaterials used in surgery in recent years has led to a significant increase in interest in tissue adhesives as an alternative to conventional wound closure methods, such as surgical sutures and mechanical staplers. Particular attention has been paid to polyurethane adhesives, which, due to their high biocompatibility and the possibility of precise tailoring of mechanical properties, are finding increasingly widespread applications in medicine. Owing to the wide range of available raw materials, it is possible to obtain materials with suitable flexibility, adhesion to moist tissues, and controlled biodegradation, making them a promising group of biomaterials intended for surgical applications. Contemporary research is focused not only on improving the mechanical properties of these materials but, above all, on endowing them with specific functionalities, including antimicrobial activity and the ability to support tissue regeneration processes [1–4].

One of the major challenges in modern surgery remains wound infections, which significantly increase the risk of postoperative complications, prolong hospitalisation time, and raise treatment costs. This issue is particularly important in procedures performed within mucosal membranes and tissues with a high degree of bacterial colonisation, such as the oral cavity, nasopharynx, and upper respiratory tract. Consequently, there is growing interest in adhesive materials that simultaneously exhibit haemostatic, sealing, and antibacterial properties [5, 6].

Tissue adhesives are currently used in numerous surgical fields, including cardiac surgery, neurosurgery, general surgery, otorhinolaryngology, and dentistry. In head and neck surgery, adhesive materials are employed to support haemostasis, seal tissues, and reduce postoperative complications following procedures involving mucosal membranes. They are of particular importance in procedures such as adenotomy, tonsillectomy, endoscopic surgery of the nose and paranasal sinuses, and reconstruction of mucosal defects, where effective protection of the surgical site may contribute to reducing the risk of secondary bleeding, limiting local inflammation, and improving the healing process. The application of modern bioadhesive materials may also contribute to reducing postoperative pain and shortening patient recovery time [7].

An important direction in the development of modern tissue adhesives is the design of materials capable of functioning effectively in moist environments, which are characteristic of most tissues in the human body. Adhesive systems based

on cyanoacrylates, albumin-based adhesives, or fibrin glues, despite their widespread clinical use, exhibit several limitations, such as insufficient flexibility or mechanical strength, the risk of local cytotoxicity, and the lack of antibacterial activity. Polyurethane adhesives represent an alternative class of materials characterised by high adhesion, suitable mechanical strength, and a controlled degradation rate [8].

In recent years, the concept of 'smart' polyurethane biomaterials has also been intensively developed. These materials are designed not only to provide mechanical wound closure but also to actively support tissue regeneration through the controlled release of bioactive substances, anti-inflammatory effects, and modulation of the body's immune response. The development of nanomaterial technologies and advanced polyurethane surface functionalisation methods opens new possibilities for designing bioactive surgical adhesives with multifunctional therapeutic effects. For this reason, antibacterial polyurethane adhesives are currently considered one of the most promising research directions in the field of modern biomedical materials and may play an important role in the future development of, among others, minimally invasive surgery and regenerative medicine [9].

In the case of polyurethane adhesives, these properties can be achieved through modification with quaternary ammonium salts, metal nanoparticles, or compounds containing hydrophilic groups. Such approaches make it possible to reduce the adhesion and proliferation of microorganisms on the biomaterial surface and decrease the risk of bacterial biofilm formation [10, 11].

Metal nanoparticle additives currently rely mostly on silver, nanosilver, or silver compounds. Some silver-free systems using nano zinc oxide, or nano titanium dioxide have been proposed. However, metal-based nanoparticles may cause aggregation, phase separation, and toxicological issues [12]. Also, combinations of silver with organic antimicrobial agents, such as quaternary ammonium compounds (QACs), are employed. QACs have the chemical structure $R_1R_2R_3R_4\ N^+X^-$ with at least one long hydrophobic hydrocarbon chain substituent that can penetrate into microbes to disrupt cell membranes. The ammonium group of QACs attracts negatively charged microbes [13]. QACs are an example of biocides active against both bacteria and enveloped viruses [14]. The interference of the lipophilic hydrocarbon chain with the envelope may potentially reduce virus infectivity [15]. A notable drawback of simple QACs, particularly those widely used, is that bacteria may develop resistance to these compounds [16].

Due to the development of bacterial resistance to these compounds, alternative solutions are being sought. In the following work, we employed the biopolymer polylysine (PLY) intercalated on montmorillonite (MM) as an antibacterial agent. Therefore, the aim of this work was to develop and characterise a polyurethane adhesive with a bio-based antibacterial agent. The study focused on understanding how the polyurethane structure and bio-based antimicrobial agent affect the mechanical and antibacterial properties of the adhesives.

2. MATERIAL AND METHODS

2.1. Materials

The following materials were used in this study:

- isophorone diisocyanate (IPDI), Evonic-Degussa (Germany),
- polyoxyethylene glycol M_n = 300 g/mol (PEG300), PCC Rokita (Poland),
- polyoxypropylenediol M_n = 750 g/mol (Rokopol 750D), PCC Rokita (Poland),
- polyoxypropylenediol M_n = 2000 g/mol (Rokopol D2002) PCC Rokita (Poland),
- triethanolamine (TEA), Aldrich (Switzerland),
- glycerine (GLY), Aldrich (Switzerland),
- dibutyltin dilaurate, Aldrich (Switzerland),
- tin octoate, Aldrich (Switzerland),
- silver phosphate (Ultra Fresh CA-16), Lexington (Malaysia),
- ε-polylysine (PLY) >95%, Mark Nature (Fullerton, CA, USA),
- sodium montmorillonite nanoclay (MM) (Sigma-Aldrich).

The intercalation of polylysine on montmorillonite was performed at the Łukasiewicz Research Network – Institute of Industrial Chemistry in Warsaw. Polyoxyethylene glycol, polyoxypropylenediols, triethanolamine, and glycerine, were dried at 110°C for 3 hours and stored over 4A molecular sieves. The other reagents were used as received.

Prepolymer synthesis

IPDI was placed in a three-necked flask equipped with a heating mantle, reflux condenser, dropping funnel, thermometer, mechanical stirrer, and nitrogen inlet tube and heated to 40°C. Polyol was then slowly added dropwise over 30 min. After adding the polyol, the reaction was carried out at 75°C until the –NCO group content reached the theoretically calculated value (about 2 hours). The reaction progress was monitored by determining the free –NCO group content using the acidimetric method. The obtained prepolymer was cooled to room temperature and poured into a container with a tight closure. The qualitative and quantitative composition of polyurethane prepolymers are presented in Table 1.

Table 1
Qualitative and quantitative composition of polyurethane prepolymers

Prepolymer symbol	Isocyanate	Isocyanate content [g/mol]	Polyol	Polyol content [g/mol]	–NCO content [%]
IPDI/PEG300	IPDI	22.2/0.1	PEG 300	15.0/0.05	11.2
IPDI/750D	IPDI	22.2/0.1	Rokopol 750D	37.5/0.05	7.2
IPDI/PEG300/D2002	IPDI	22.2/0.1	PEG 300 Rokopol D2002	7.5/0.025 50.0/0.025	5.3

Preparation of adhesive samples

Samples of adhesives were obtained by mixing the prepolymers first with the antimicrobial agent (silver phosphate or PLY/MM) and then with a cross-linking agent and the catalyst. The cross-linking agents were glycerine or triethanolamine. The amount of cross-linking agent was adjusted to obtain a molar ratio of –NCO:OH groups of 1.10:1. Dibutyltin dilaurate or tin octoate was used as the catalyst at a concentration of 0.02%. All ingredients were mixed with a mechanical stirrer in a closed flask at room temperature for 2 minutes. The mixture was then poured into silicone moulds and allowed to cure in a desiccator with 90% humidity. Gelation began after approximately 10 minutes, and curing occurred after approximately 30 minutes, regardless of the composition.

2.2. Methods

The adhesive was characterised using the following methods.

Gel permeation chromatography (GPC)

Gel permeation chromatography (GPC) studies were performed using an Agilent 1100 Series liquid chromatograph equipped with a G1379A degasser, a G1311A four-channel QuatPomp pump, a G11316A column thermostat, a VARIAN PLGEL 5#M MIXED-D chromatography column (*dp* = 5 µm, column dimensions 300 × 7.5 mm) and dedicated precolumn, an RID G1362A refractometric detector, and a valve injector with a 20 µL loop. Analyses were performed at 35°C with a mobile phase (THF) volumetric flow rate of 1 ml/min.

Viscosity tests

A Brookfield CAP 2000+ viscometer was used to test viscosity.

Hardness tests

Hardness tests was carried out in accordance with the PN-EN ISO 868 standard, using a Shore A hardness tester.

Strength tests

The tensile strength and percentage elongation of the hardened castings were determined on an INSTRON 5967 universal testing machine. The measurement was performed under a load of 5 kN and a crosshead speed of 20 mm/min at room temperature.

Water contact angle tests

Water contact angle measurements were performed using a Data Physic optical goniometer, model OCA 15, according to the ISO 19403 standard.

Fourier-transform infrared spectroscopy (FTIR)

FTIR analysis was performed using a Nicolet™ iS™ 10 FTIR spectrometer using the ATR technique.

Antibacterial tests

Antibacterial properties were tested according to the ISO 22196 standard on E. Coli and S. Aureus bacteria.

Adhesion tests

The adhesion of the adhesive to pig tissue was tested by the pull-off method using a PosiTest AT-A Automatic Adhesion Tester.

3. RESULTS AND DISCUSSION

Isophorone diisocyanate (IPDI) was used for the synthesis of the adhesives due to its cycloaliphatic structure, which imparts flexibility and exhibits lower toxicity compared to aromatic polyisocyanates. Aliphatic polyoxy glycols with different molecular weights were selected as the polyol component. The molar ratio of isocyanate to polyol was 2:1. During the synthesis of the IPDI/PEG300 prepolymer, uncontrolled gelation of the product occurred. The molecular weight distribution was analysed using gel permeation chromatography (GPC). Examples of GPC chromatograms are shown in Figure 1.

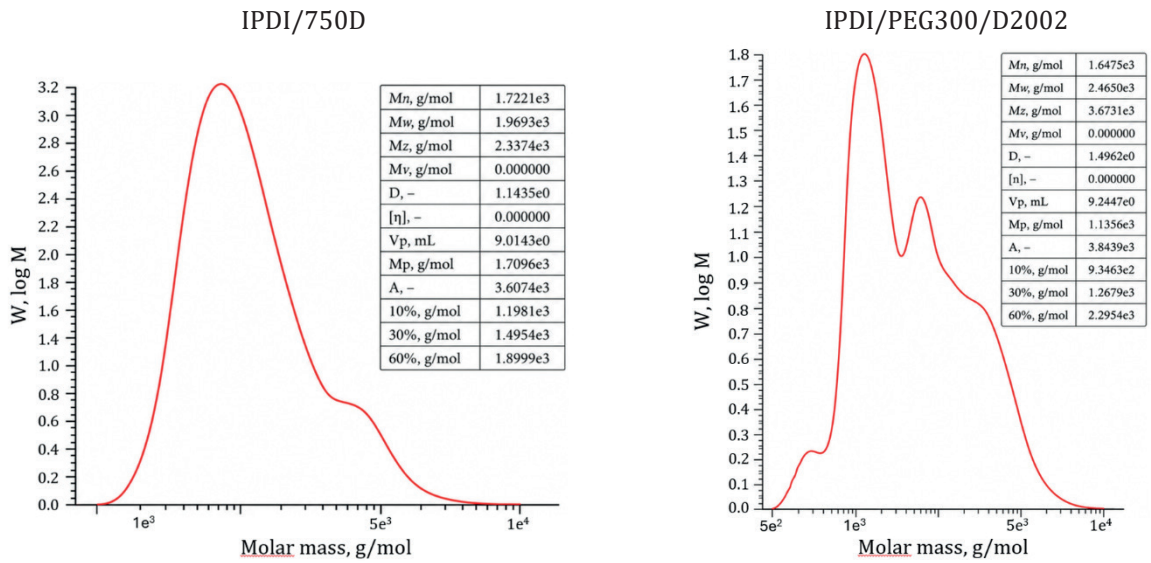

Fig. 1. GPC chromatograms of IPDI/750D and IPDI/PEG300/D2002 prepolymers

Based on the obtained GPC chromatograms, the average molecular weights and dispersity index of the prepolymers were determined (Table 2).

In the chromatograms, in addition to the signal corresponding to the main product resulting from the reaction stoichiometry (a prepolymer with the IPDI–polyol–IPDI structure), products with higher molecular weights were also observed, which is typical for prepolymer synthesis via polyaddition reactions. The dispersity index (PD) values were 1.14 and 1.5, indicating a relatively narrow molecular weight distribution. Both obtained prepolymers exhibited relatively low viscosity values (Table 2), which is advantageous during dosing, mixing, and spreading of the adhesive on tissues.

Glycerine or triethanolamine, together with organotin catalysts, was used as the crosslinking agent for the adhesives. The molar ratio of prepolymer –NCO groups to the OH groups of the crosslinking agent was 1.10:1. Attempts to crosslink the adhesives in the presence of amine catalysts resulted in product foaming due to accelerated catalysis of the competing reaction with moisture, leading to carbon dioxide evolution. The course of the adhesive crosslinking process using glycerine is shown in Figure 2.

The crosslinked IPDI/PEG300/D2002 sample was brittle and prone to fracture; therefore, only the IPDI/750D/GLY and IPDI/750D/TEA compositions were selected for further studies. Formulations containing silver phosphate and polylysine intercalated in montmorillonite (PLY/MM) were prepared (Table 3).

After crosslinking, the best properties were exhibited by the glycerine-crosslinked formulations prepared in the presence of dibutyltin dilaurate as the catalyst, namely IPDI/750D/GLY/Ag/DSn and IPDI/750D/GLY/PLY/MM/DSn (Fig. 3).

Table 2
GPC results and viscosity of polyurethane prepolymers

Prepolymer	M_n [g/mol]	M_w [g/mol]	PD	Viscosity [Pa·s]
IPDI/750D	1722.1	1969.3	1.14	2.30
IPDI/PEG300/D2002	1647.5	2465.0	1.50	3.36

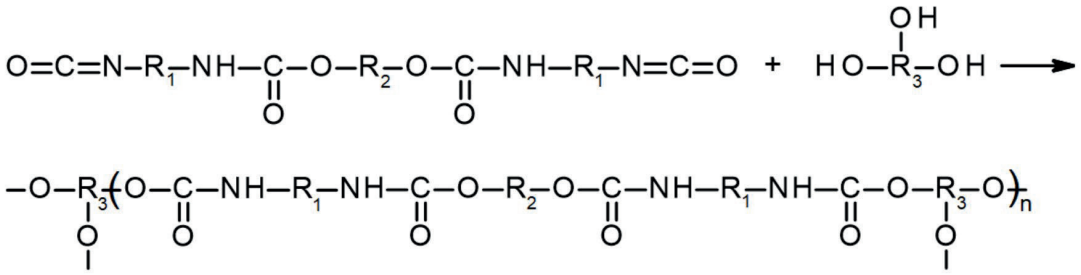

Fig. 2. Course of the prepolymer crosslinking reaction using glycerine or triethanolamine

Table 3
Qualitative and quantitative composition of polyurethane adhesives

No.	Sample symbol	Prepolymer	Curing agent	Antimicrobial agent [%]	Catalyst [%]
1	IPDI/750D/GLY/Ag/OSn	IPDI/750D	glycerine (GLY)	Ag_3PO_4 (Ag), 0.5	tin octoate (OSn)/0.02
2	IPDI/750D/GLY/PLY/MM/OSn	IPDI/750D	glycerine (GLY)	PLY/MM, 2.0	tin octoate (OSn)/0.02
3	IPDI/750D/TEA/Ag/DSn	IPDI/750D	triethanolamine (TEA)	Ag_3PO_4 (Ag), 0.5	dibutyltin dilaurate (DSn)/0.02
4	IPDI/750D/TEA/PLY/MM/DSn	IPDI/750D	triethanolamine (TEA)	PLY/MM, 2.0	dibutyltin dilaurate (DSn) 0.02
5	IPDI/750D/GLY/Ag/DSn	IPDI/750D	glycerine (GLY)	Ag_3PO_4(Ag), 0.5	dibutyltin dilaurate (DSn) 0.02
6	IPDI/750D/GLY/PLY/MM/DSn	IPDI/750D	glycerine (GLY)	PLY/MM, 2.0	dibutyltin dilaurate (DSn) 0.02

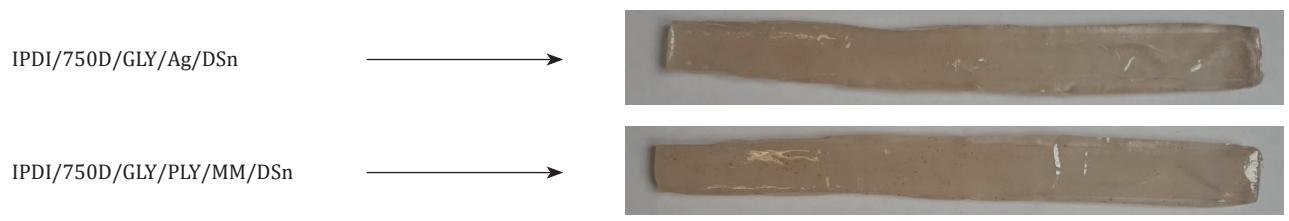

Fig. 3. Appearance of adhesive samples after cross-linking

The structure of the crosslinked adhesives was confirmed using FTIR spectroscopy (Fig. 4).

The band at 3300 cm^{-1} is characteristic of N–H stretching vibrations, the band at 1700 cm^{-1} corresponds to C=O stretching vibrations, while the signal in the 1550 cm^{-1} region is attributed to N–H bending vibrations, confirming the presence of urethane groups. No absorption band at 2200 cm^{-1}, assigned to isocyanate groups, was observed in the spectra, indicating their complete conversion into urethane linkages.

The measured Shore A hardness and tensile strength values of the adhesives are presented in Figure 5 and Table 4.

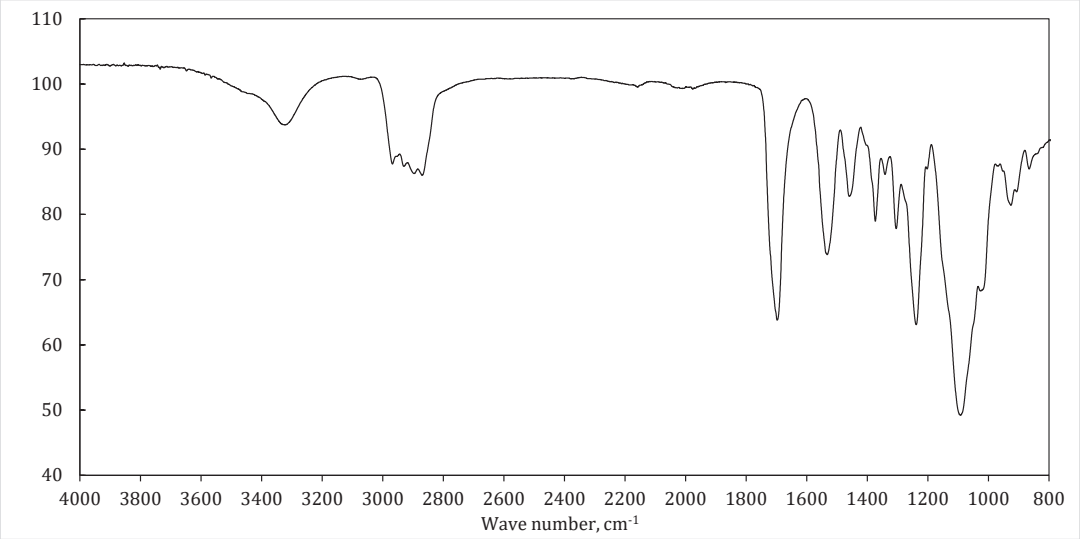

Fig. 4. FTIR spectrum of IPDI/750D/GLY/Ag/DSn adhesive

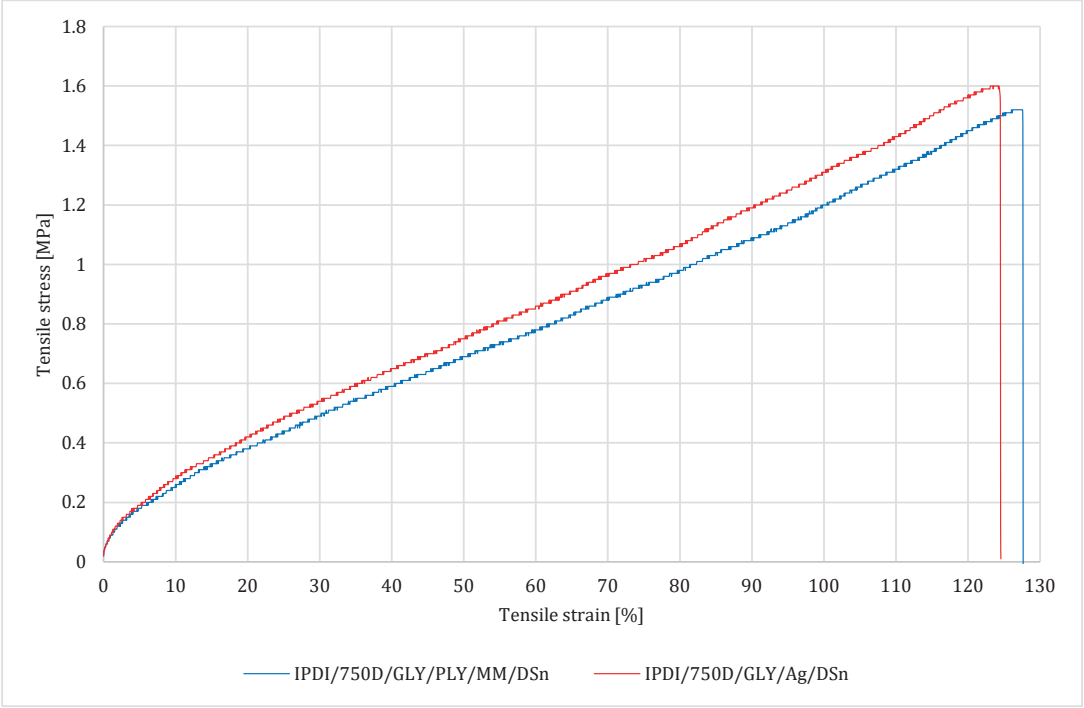

Fig. 5. Tensile stress–strain curves of adhesives IPDI/750D/GLY/Ag/DSn and IPDI/750D/GLY/PLY/MM/DSn

Table 4
Summary of Shore A hardness and tensile strength values of adhesives

Sample symbol	Hardness Shore A	Tensile strength [MPa]	Strain at break [%]	Young's Modulus [GPa]
IPDI/750D/GLY/Ag/DSn	35	1.60	124	1.96
IPDI/750D/GLY/PLY/MM/DSn	36	1.52	128	1.95

The hardness and tensile strength results indicate good mechanical strength and elasticity of the adhesives, which is highly advantageous for accommodating tissue movement.

The tensile bond strength of porcine tissue joints was 5.94 MPa (Fig. 6). At this value, failure occurred first at the fixture (grip detachment), while neither adhesive nor cohesive failure of the tissue specimens was observed. This indicates that the synthesised adhesive is resistant to tensile stresses exceeding the measured value.

Fig. 6. A sample of bonded porcine tissues prepared for pull-off adhesion testing

The contact angle values of all four adhesives were below 90°, indicating that the obtained materials are hydrophilic (Fig. 7). This property may promote improved adhesion of the adhesive to skin. Comparing the contact angle values, it can be observed that the lowest value was obtained for the glycerine-cured adhesive containing silver phosphate as the antibacterial additive. This is attributed to the more hydrophilic nature of both glycerine and Ag_3PO_4 compared to triethanolamine and polylysine.

The results of the antibacterial tests are presented in Table 5.

The conducted studies indicate that polylysine exhibits superior antibacterial properties. The percentage reduction values for this agent exceeded 99%, indicating that *Escherichia coli* and *Staphylococcus aureus* cells were almost completely eliminated. The percentage reduction value for Ag_3PO_4 reached 38.55%, which indicates approximately a threefold lower effectiveness of this commonly used biocide. Higher antibacterial activity of polylysine compared to Ag_3PO_4 was also observed in the case of modifications of other polymers [17].

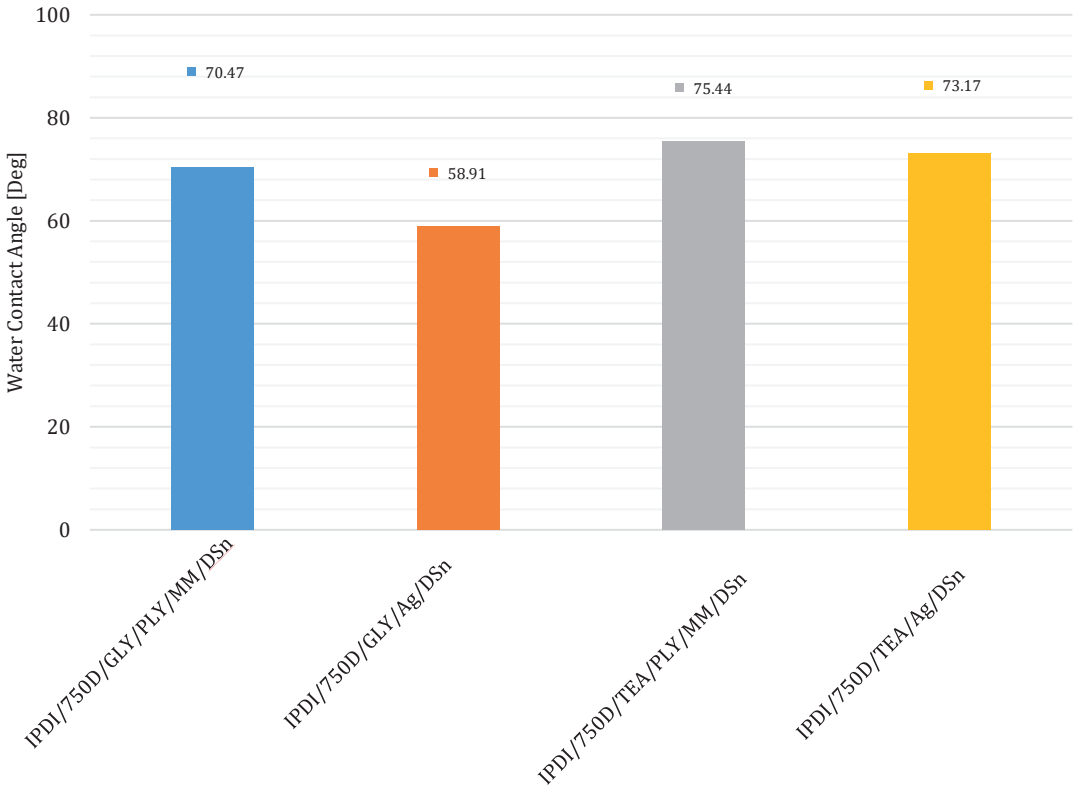

Fig. 7. Water contact angle of IPDI/750D prepolymer-based adhesive

Table 5
Summary of antibacterial activity results

Sample symbol	Antimicrobial agent	Bacteria	% reduction	Log reduction
IPDI/750D/GLY/Ag/DSn	Ag_3PO_4	*S. Aureus*	38.5511	0.21
IPDI/750D/GLY/PLY/MM/DSn	PLY/MM	*E. Coli*	99.9984	4.80
IPDI/750D/GLY/PLY/MM/DSn	PLY/MM	*S. Aureus*	99.7330	2.57

4. CONCLUSIONS

As part of the conducted studies, polyurethane prepolymers and two-component adhesive systems exhibiting antibacterial properties were synthesised. The obtained materials were characterised by favourable rheological properties: the viscosity of the prepolymers, measured using a Brookfield viscometer, ranged from 2.30 to 3.36 Pa·s, indicating good processability, ease of dosing, and applicability to tissue surfaces.

Confirmation of the chemical structure of the crosslinked adhesives was obtained through FTIR spectroscopy analysis, which demonstrated the presence of characteristic urethane groups and the complete conversion of isocyanate groups. Contact angle measurements revealed the hydrophilic nature of the obtained materials, which may promote good adhesion to moist biological tissues.

Mechanical testing showed that the developed adhesives exhibit medium hardness (so-called medium-soft materials), which is a desirable feature in medical applications where mechanical compatibility with tissues is essential. At the same time, the adhesive bond strength exceeding 5 MPa indicates high adhesion to tissues and effective sealing of the application site.

The conducted tests also demonstrated that the applied biopolymer-based antibacterial agent exhibits very high biocidal efficiency, representing a promising alternative to commonly used silver compounds.

Future research will focus on optimising the adhesive composition in order to tailor its mechanical properties to different types of tissues. It will also be important to extend the study to investigate biodegradation under in vitro and in vivo conditions. Additionally, determining the release kinetics and duration of antibacterial activity of the additives in a biological environment will be a key aspect of further investigations.

ACKNOWLEDGEMENTS

The authors would like to thank PCC Rokita and Evonic-Degussa for sending free samples of raw materials, and Michał Kędzierski PhD Eng. for performing the intercalation of polylysine on MMT.

REFERENCES

[1] Zhu S., Dou W., Zeng X., Chen X., Gao Y., Liu H. & Li S. (2024). Recent advances in the degradability and applications of tissue adhesives based on biodegradable polymers. International Journal of Molecular Sciences, 25(10), 5249. DOI: https://doi.org/10.3390/ijms25105249.

[2] Han G.Y., Hwang S.K., Cho K.H., Kim H.J. & Cho C.S. (2023). Progress of tissue adhesives based on proteins and synthetic polymers. *Biomaterials Research*, 27(1), 57. DOI: https://doi.org/10.1186/s40824-023-00397-4.

[3] Zhou Q., Shi Z., Xia L., Mi J., Zhang Y., Xu X. & Pan J. (2024). Breaking the boundaries of wound closure: A novel polyurethane tissue adhesive with enhanced healing properties. *Journal of Biomedical Materials Research Part A*, 112 (12), 2301–2313. DOI: https://doi.org/10.1002/jbm.a.37770.

[4] Youn J., Patel K.D., Perriman A.W., Sung J.-S., Patel, Bouchard L.-S. & Patel R. (2024). Tissue adhesives based on chitosan for biomedical applications. *Journal of Materials Chemistry B*, 12(41), 10446–10465. DOI: https://doi.org/10.1039/D4TB01362J.

[5] Sim N., Lee H., Goyal N. & Cramer J.D. (2024). Surgical site antiseptic preparations for otolaryngology – head and neck surgery: A current review. *American Journal of Otolaryngology*, 45(4), 104280. DOI: https://doi.org/10.1016/j.amjoto.2024.104280.

[6] Zhang H., Feng Y., Wang T., Zhang J., Song Y., Zhang J., Li Y., Zhou D. & Gu Z. (2024). Natural polyphenolic antibacterial bio-adhesives for infected wound healing. *Biomaterials Science*, 12(9), 2282–2291. DOI: https://doi.org/10.1039/D3BM02122J.

[7] Olzowy B., Müller S., Cidlinsky N.A. & Guderian D. (2024). Antiseptics in otorhinolaryngology – a substance overview. *HNO*, 72, 452–460. DOI: https://doi.org/10.1007/s00106-024-01456-5.

[8] Gerardi D., Burdo P., Turkyilmaz I., Diomede F., Mendes G.D., Piattelli M. & Varvara G. (2025). Clinical applications and efficacy of cyanoacrylates in oral surgery and periodontology: a scoping review. *Medicina*, 61(7), 1286. DOI: https://doi.org/10.3390/medicina61071286.

[9] Zhang J., Lv S., Zhao X., Ma S. & Zhou F. (2024). Surface functionalization of polyurethanes: a critical review. *Advances in Colloid and Interface Science*, 325, 103100. DOI: https://doi.org/10.1016/j.cis.2024.103100.

[10] Guo X., Wang A., Sheng N., He Y., Liu W., Li Z., Luo F., Li J. & Tan H. (2024). Janus polyurethane adhesive patch with antibacterial properties for wound healing. *ACS Applied Materials & Interfaces*, 16(13), 15970–15980. DOI: https://doi.org/10.1021/acsami.4c00924.

[11] Drożdż K., Gołda-Cępa M. & Brzychczy-Włoch M. (2024). Polyurethanes as biomaterials in medicine: advanced applications, infection challenges, and innovative surface modification methods, *Advancements of* Microbiology, 63(4), 223–238. DOI: https://doi.org/10.2478/am-2024-0018.

[12] Yao Y. , Zang Y., Qu J., Tang M. & Zhang T. (2019). The toxicity of metallic nanoparticles on liver: the subcellular damages, mechanisms, and outcomes. *International Journal of Nanomedicine*, 14, 8787–8804. DOI: https://doi.org/10.2147/IJN.S212907.

[13] Li F. , Weir M.D. & Xu H.H.K. (2013). Effects of quaternary ammonium chain length on antibacterial bonding agents. *Journal of Dental Research*, 92(10), 932–938. DOI: https://doi.org/10.1177/0022034513502053.

[14] Baker N., Williams A.J., Tropsha A. & Ekins S. (2020). Repurposing quaternary ammonium compounds as potential treatments for COVID-19. *Pharmaceutical Research*, 37, 104. DOI: https://doi.org/10.1007/s11095-020-02842-8.

[15] Lin Q., Lim J.Y.C., Xue K., Yew P.Y.M., Owh C., Chee P.L. & Loh X.J. (2020). Sanitizing agents for virus inactivation and disinfection. *View*, 1(2), e16. DOI: https://doi.org/10.1002/viw2.16.

[16] Hegstad K., Langsrud S., Sheie A.A., Sunde M. & Yazdankhah S.P. (2010). Does the wide use of quaternary ammonium compounds enhance the selection and spread of antimicrobial resistance and thus threaten our health? *Microbial Drug Resistance*, 16(2), 91–104. DOI: https://doi.org/10.1089/mdr.2009.0120.

[17] Krawczyk K., Pilch-Pitera B., Kędzierski M., Zubilewicz M., Langer E., Jurczyk S., Kamińska-Bach G., Daszykowska K., Komorowski L., Bieniek K., Przybysz-Romatowska M. & Hilt M. (2025). Antimicrobial activity of silver free powder coatings based on biocomponents. *Scientific Reports*, 15, 43021. DOI: https://doi.org/10.1038/s41598-025-30166-3.